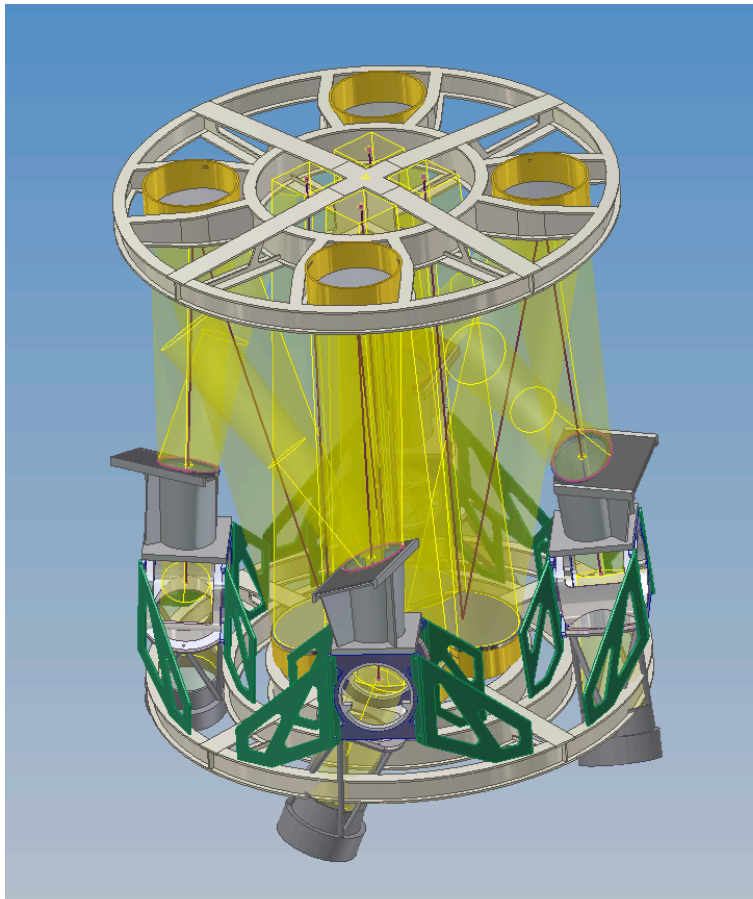


TMT Wide-Field Optical Spectrograph Operational Concepts Definition Document

Roberto G. Abraham, Jarle Brinchmann, J. Christopher Clemens,
Patrick Côté, Sara L. Ellison, Karl Glazebrook, Raja Guhathakurta,
Michael J. Hudson, Jasonjot S. Kalirai, Eric W. Peng,
Charles C. Steidel, Marten H. van Kerkwijk



September 23, 2005

| Revision | Date | Author | Description |
|----------|------------------|------------------|-----------------------------------|
| 0.0 | July 9, 2005 | RGA | Initial outline |
| 0.1 | Aug 8–12, 2005 | PC/EP/SE/RGA/JB | Started science cases |
| 0.20 | Aug 19–23, 2005 | SE/CCS | Improved tomography case |
| 0.21 | Aug 19–23, 2005 | RGA | Tweaks to f_{esc} case |
| 0.22 | Aug 19–23, 2005 | JK | Added stellar evolution case |
| 0.3 | Sept 1, 2005 | PC | Tweaks to DM case |
| 0.4 | Sept 8, 2005 | RGA/PC | Sections 1, 3, 5 added |
| 0.5 | Sept 9, 2005 | RGA | Section 7 added |
| 0.6 | Sept 10–12, 2005 | RGA | Global smoothing |
| 0.7 | Sept 14, 2005 | CCS/SE | Improved tomography case |
| 0.8 | Sept 15, 2005 | PC | Revisions and polishing |
| 0.90 | Sept 16, 2005 | RGA | More revisions and polishing |
| 0.91 | Sept 22, 2005 | PC | Resolved stellar populations case |
| 0.92 | Sept 22, 2005 | RGA/KGB | Infrared arm case |
| 1.0 | Sept 23, 2005 | SE/JB/CCS/JK/RGA | Revisions in response to v.0.90 |

Contents

| | | |
|----------|--|-----------|
| 1 | Introduction | 6 |
| 1.1 | Purpose of this document | 6 |
| 1.2 | How to read this document | 6 |
| 1.3 | Acronyms | 7 |
| 1.4 | Acknowledgments | 7 |
| 2 | Instrument Description | 8 |
| 2.1 | Overview | 8 |
| 2.2 | Summary of Requirements | 8 |
| 2.2.1 | Modes of operation | 8 |
| 2.2.2 | Field of view | 9 |
| 2.2.3 | Resolution | 9 |
| 2.2.4 | Wavelength coverage | 10 |
| 2.2.5 | Image quality | 10 |
| 2.2.6 | PSF uniformity and stability | 11 |
| 2.2.7 | Field distortion | 11 |
| 2.2.8 | Throughput | 11 |
| 2.2.9 | Observing efficiency | 12 |
| 2.2.10 | Ground-Layer Adaptive Optics (GLAO) | 12 |
| 3 | Sample Observing Scenarios | 13 |
| 3.1 | Stellar Evolution and White Dwarfs | 13 |
| 3.1.1 | Background | 13 |
| 3.1.2 | Specific science goals | 14 |
| 3.1.3 | Observations and Targets | 16 |
| 3.1.4 | Pre-imaging | 17 |
| 3.1.5 | Technical Remarks and Mask Design | 17 |
| 3.1.6 | Path to Science | 20 |
| 3.2 | Resolved Stellar Populations in the Local Group | 22 |
| 3.2.1 | Background | 22 |
| 3.2.2 | Planning of observations | 23 |
| 3.2.3 | Pre-imaging | 27 |
| 3.2.4 | Mask design | 27 |
| 3.2.5 | Procedures during the day | 27 |
| 3.2.6 | Procedures during twilight | 27 |
| 3.2.7 | Target acquisition | 27 |
| 3.2.8 | Target science data acquisition | 27 |
| 3.2.9 | Calibration data acquisition | 29 |
| 3.2.10 | Facility requirements | 29 |
| 3.3 | The Dark Matter Distribution in Nearby Elliptical Galaxies | 30 |
| 3.3.1 | Background | 30 |
| 3.3.2 | Planning of observations | 31 |
| 3.3.3 | Pre-imaging | 34 |
| 3.3.4 | Mask design | 34 |

| | | |
|----------|---|-----------|
| 3.3.5 | Procedures during the day | 37 |
| 3.3.6 | Procedures during twilight | 37 |
| 3.3.7 | Target acquisition | 37 |
| 3.3.8 | Target science data acquisition | 37 |
| 3.3.9 | Calibration data acquisition | 38 |
| 3.3.10 | Facility requirements | 38 |
| 3.4 | Observing Three-Dimensional Baryonic Structure During the Epoch of Galaxy Formation | 39 |
| 3.4.1 | Background | 39 |
| 3.4.2 | Specific science goals | 41 |
| 3.4.3 | Planning of observations | 41 |
| 3.4.4 | Pre-imaging | 46 |
| 3.4.5 | Mask design | 47 |
| 3.4.6 | Procedures during the day | 48 |
| 3.4.7 | Procedures during twilight | 48 |
| 3.4.8 | Target acquisition | 48 |
| 3.4.9 | Target science data acquisition | 49 |
| 3.4.10 | Calibration data acquisition | 49 |
| 3.4.11 | Additional requirements | 49 |
| 3.5 | Astrophysics of primordial galaxies | 52 |
| 3.5.1 | Science justification and background | 52 |
| 3.5.2 | Key observable: the escape fraction of UV photons at $z \sim 6$ | 53 |
| 3.5.3 | Sample definition | 53 |
| 3.5.4 | Pre-imaging | 54 |
| 3.5.5 | Mask design | 54 |
| 3.5.6 | Required integration time | 55 |
| 3.5.7 | Procedures during the day | 56 |
| 3.5.8 | Procedures during twilight | 56 |
| 3.5.9 | Target acquisition | 56 |
| 3.5.10 | Sky subtraction, CCD device characteristics, and shutter operation | 56 |
| 3.5.11 | Calibration data acquisition | 57 |
| 3.5.12 | Facility requirements | 57 |
| 4 | Calibration Procedures | 58 |
| 4.1 | Geometric distortion | 58 |
| 4.2 | Flat-field and bias | 58 |
| 4.3 | Wavelength calibration | 59 |
| 4.4 | Flux calibration | 59 |
| 4.5 | Linearity | 60 |
| 4.6 | Dark current | 60 |
| 4.7 | Telluric absorption | 60 |

| | | |
|----------|---|-----------|
| 5 | Summary: Building the Spectrograph We Want | 62 |
| 5.1 | Desired improvements | 62 |
| 5.2 | Science value of GLAO to WFOS | 62 |
| 5.3 | Science value of IR arm to WFOS | 63 |
| 5.4 | GLAO vs. SLGLAO | 63 |
| 5.5 | Future changes in this document | 63 |
| 6 | References | 65 |

1 Introduction

1.1 Purpose of this document

This document presents selected science drivers for a proposed Wide-Field Optical Spectrograph (WFOS) for the Thirty Meter Telescope (TMT). It relates the science requirements to the instrument concepts under consideration. It also identifies the key operational scenarios, outlines observation procedures, and describes the required interactions between WFOS, the telescope system, and the observatory. These operational scenarios are described in sufficient detail to allow technical judgments with respect to their feasibility to be made. The background science cases are presented at a level that is intended to be intelligible to a non-astronomically-expert but scientifically literate systems engineer (our target audience).

1.2 How to read this document

A brief description of WFOS is given in Section 2. Readers who are already very familiar with the WFOS design can skip this section. Conversely, readers who are completely new to WFOS and who are looking for a very detailed description of the spectrograph are referred to the WFOS Functional and Performance Requirements Document (FPRD).

The sample observing scenarios which form the heart of the document are given in Section 3. It is important to note that the science cases in this Section were purposely chosen to stretch the design envelope for WFOS and to exercise most of the modes of the instrument, rather than in a (hopeless) attempt to anticipate all the most important science that will be undertaken with WFOS ten years in the future. In choosing science cases an attempt was also made to select example programs that are unlikely to be achievable in the next decade with any existing (or planned) ground-based or space-based facility. To avoid needless repetition, those aspects of the observing scenarios that are common to all science cases (such as global calibrations) are dealt with in Section 4. An attempt to summarize Sections 3 and 4 into a requirements flow-down is presented in Section 5.

WFOS has been designed as a general purpose instrument with a broad range of capabilities, but of course the design of any large spectrograph requires that choices be made when optimizing the instrument. In some cases optimizing the design for the efficient execution of one science program can mean trading off some efficiency in accomplishing other programs. In such cases the the WFOS Design Team has globally optimized for the efficiency of the ‘IGM tomography’ case explored in Section 3.4. Our rationale for this is based on a belief that this particular science case will almost certainly be a ‘key project’ for TMT, coupled with the reality that a very large number of nights will be required to accomplish it. The reader may therefore wish to pay particular attention to Section 3.4.

1.3 Acronyms

| | |
|--------|---|
| AGN | Active Galactic Nuclei |
| ADC | Atmospheric Dispersion Compensator |
| AO | Adaptive Optics |
| CFHT | Canada France Hawaii Telescope |
| CDM | Cold Dark Matter |
| CMD | Color Magnitude Diagram |
| DHS | Data Handling System |
| DM | Deformable Mirror |
| EE | Encircled Energy |
| FOV | Field of View |
| FPRD | Functional and Performance Requirements Document |
| FWHM | Full Width Half Maximum |
| GC | Globular Cluster |
| GLAO | Ground-Layer Adaptive Optics |
| GMOS | Gemini Multi-Object Spectrograph |
| HST | Hubble Space Telescope |
| IGM | Intergalactic Medium |
| IR | Infrared |
| LGS | Laser Guider Star |
| NIFS | Near-Infrared Integral-Field Spectrograph |
| OCDD | Operational Concept Definition Document (this document) |
| OCS | Observatory Control System |
| OICS | On-instrument Control System |
| OIWFS | On-instrument Wavefront Sensor |
| PN | Planetary Nebula |
| PSF | Point-Spread Function |
| QSO | Quasi Stellar Object |
| RMS | Root Mean Square |
| SDSS | Sloan Digital Sky Survey |
| SLGLAO | Single-Laser Ground-Layer Adaptive Optics (pronounced ‘Sly-Go’) |
| TCS | Telescope Control System |
| TMT | Thirty Meter Telescope |
| WFOS | Wide-Field Optical Spectrograph |
| WMAP | Wilkinson Microwave Anisotropy Probe |

1.4 Acknowledgments

The structure of this document is based heavily on the GMOS, NIFS, Flamingos-2, F2T2 and GMOS Nod & Shuffle Mode OCDDs. We thank Tim Davidge and Steve Eikenberry for allowing us to borrow heavily from the calibration portions of the GMOS and Flamingos-2 OCDDs .

2 Instrument Description

2.1 Overview

WFOS is a seeing-limited multi-object imaging spectrograph designed to perform multi-object spectroscopy and imaging of faint sources over a large field (≥ 100 arcmin²) with high throughput ($\geq 30\%$), high slit density (i.e., comparable to or better than those achieved by the current generation of multi-object spectrographs on 8m-class telescopes) and high operational efficiency over the complete wavelength range from the near-UV to the near infrared. The device will occupy a fixed location on one of the TMT Nasmyth platforms. It will be fed directly at the Gregorian focus by the telescope beam redirected from an articulated telescope tertiary mirror. The instrument will be able to rotate to compensate for relative field rotation. Since no acquisition, guiding, or calibration systems are currently planned for the TMT facility, these capabilities will be included in the WFOS instrument through the use of an on-instrument wavefront sensor (OIWFS) which interfaces to the telescope control system (TCS) and secondary mirror. To enhance image quality, the WFOS design will incorporate an atmospheric dispersion compensator (ADC), as well as a guiding system and active optics. For reasons of efficiency, the field of view of WFOS is broken into four separate zones, each of which is fed into a separate spectrograph. Each spectrograph is in turn separated into red and blue camera paths using dichroic beam splitters. The optical design of WFOS is illustrated in Figures 1 and 2. The opto-mechanical layout of the instrument is shown as a 3D CAD drawing on the cover page of this document.

WFOS will be controlled by an on-instrument control system (OICS) that will interface to the TMT observatory control system (OCS) and data handling system (DHS). WFOS will incorporate a robust structure to support the various components of the instrument and minimize instrument flexure. In addition, it will incorporate an enclosure to protect its components and provide a light tight environment for the optical elements. The basic design of the support structure and enclosure will also offer ready access to all configurable portions of the instrument, such as the ADC, slit masks, dichroics, filters, gratings, and detectors to facilitate set-up and maintenance.

The instrumental design includes an optional ground-layer adaptive optics (GLAO) system to improve upon the natural seeing image quality. This system is intended to interface with the TMT laser guide star (LGS) system and the adaptive secondary mirror. Because the adaptive secondary mirror is not expected to be available at first light, alternative AO constructs using on-instrument deformable mirrors, such as Single Laser Ground-Layer Adaptive Optics (SLGLAO) are also considered in the design.

2.2 Summary of Requirements

2.2.1 Modes of operation

WFOS has three modes of operation: direct imaging, longslit spectroscopy and multi-object spectroscopy. To achieve the maximum observing efficiency and maintain TMT's aperture advantage over current telescopes, it must be possible to switch between modes with minimal downtime. The WFOS design should not exclude the possibil-

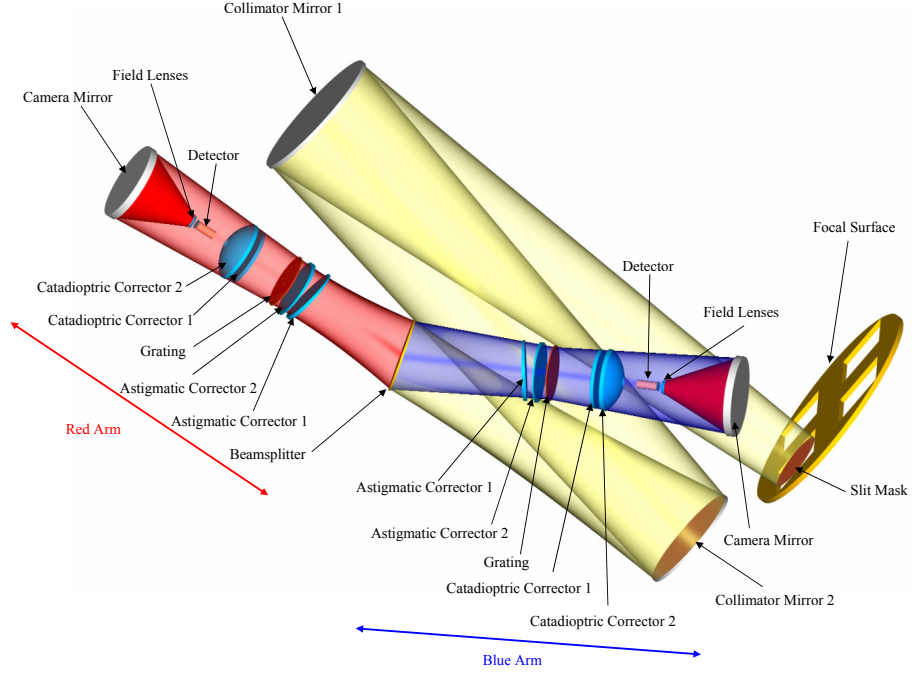


Figure 1: Optical layout of one barrel of the WFOS reference design, including the separate red and blue arms. All optical components, and key mechanical elements, have been labelled.

ity of adding an integral field unit (IFU) mode.

2.2.2 Field of view

The field of view requirement on WFOS is $\geq 75 \text{ arcmin}^2$. The current WFOS design delivers a field of view of 104 arcmin^2 , divided equally among four 26 arcmin^2 barrels. The total slit length delivered by this design is $4 \times 380'' \approx 1520''$, a three-fold improvement over the requirement of $\geq 500''$. The layout of the WFOS focal plane is shown in Figure 3.

2.2.3 Resolution

The science drivers require WFOS resolutions in the range $\mathcal{R} = 500 - 5000$. For WFOS to be versatile enough to meet the resolution and observing efficiency requirements of the individual science programs, six deployable gratings per camera will be interchangeably mounted in an automated manner at each collimator pupil during a night's observation.

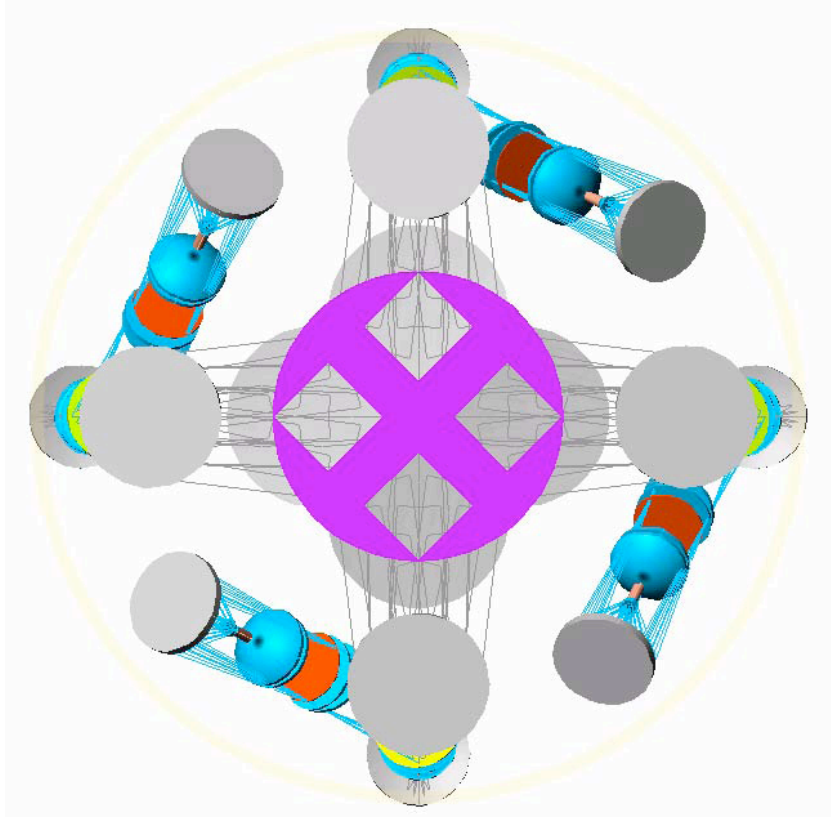


Figure 2: *Optical layout of WFOS viewed from above the focal plane. This illustrates the packing of the collimator mirrors relative to the focal plane arrangement. Note that the focal plane is divided into four separate zones each of which is fed into a separate barrel of the spectrograph.*

2.2.4 Wavelength coverage

The science drivers require WFOS to provide continuous, and sometimes simultaneous, wavelength coverage over the range $0.34\text{--}1.0\mu\text{m}$. The highest efficiency and scientific flexibility is achieved by separating the light to each barrel into red and blue camera paths with the aid of dichroic beam splitters.

2.2.5 Image quality

It is required that the image quality of WFOS in imaging mode be $\leq 0''.2$ FWHM over any $0.1\mu\text{m}$ interval; in spectrograph mode, the image quality requirement is $\leq 0''.2$ FWHM at every wavelength. Several science programs will benefit from the ADC which has been integrated into the WFOS design.

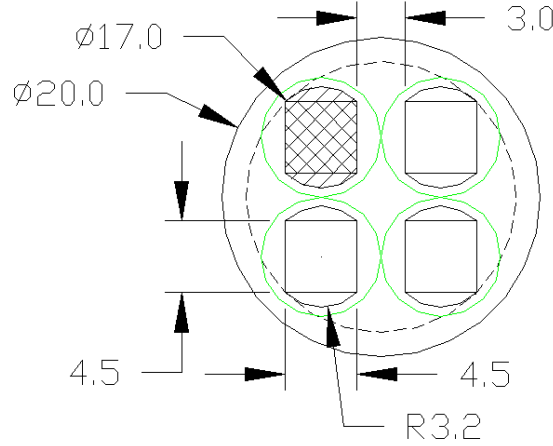


Figure 3: The WFOS focal plane. Labels correspond to dimensions projected onto the plane of the sky in units of arcminutes. The cross-hatched squares are 4.5×4.5 in size, and divide the focal plane into four separate zones, each of which is fed into a separate barrel of the spectrograph. Throughout this document we assume the instrument has a 4.5×4.5 field of view defined by these regions. The diagonal shaded regions are extensions to the field of view currently being explored by the engineering team. The green circles are boundaries set by the ADC and collimator mirror footprints that set physical limits on how closely the focal planes of the individual WFOS barrels can be packed.

2.2.6 PSF uniformity and stability

The PSF uniformity is affected by both telescope/instrument aberrations and any ground-layer adaptive optics (GLAO) system. It is required that the PSF should be uniform to the level of $\lesssim 5\%$ in FWHM over the $0.34 - 1.0\mu m$ range, independent of the decision to implement (GLAO). The instrument and GLAO architectures should not exacerbate the time variability of turbulence strength on timescales of one hour or less.

2.2.7 Field distortion

Field distortion at the camera image must be small enough to not contribute to instrument performance loss. To satisfy this requirement, it must be possible to map the distortion for extraction routines and mask design. Spectral slope and rotation due to field distortion should not cause pixelation errors in the extraction.

2.2.8 Throughput

For WFOS to capitalize on the aperture advantage of TMT compared to existing facilities, it must achieve a minimum throughput of 30% over the $0.34-1.0\mu m$ wavelength range.

2.2.9 Observing efficiency

As a general-purpose instrument, WFOS will be used for many different science programs over its lifetime, many of which will be surveys of one sort or another. Observing efficiency is therefore crucial, and we expect that WFOS will be required to switch between modes and be reconfigured several times on a typical night. Such reconfigurations must be made without affecting the basic setup and internal alignment of the spectrograph. Given that WFOS will be reconfigured automatically during the night, and acquire numerous set-up and calibration images, it is critical that any time lost due to these functions be minimized.

2.2.10 Ground-Layer Adaptive Optics (GLAO)

Almost all science programs will benefit from a ground-layer adaptive optics (GLAO) system, either directly via enhanced image quality and observing efficiency, or indirectly by making it more probable that a given set of observations will be turned to in a queue. An optional GLAO system which uses an adaptive secondary mirror and a constellation of five laser guide stars positioned outside of the science field has been included in the WFOS design.

3 Sample Observing Scenarios

In this section we analyze the following set of representative observing scenarios:

- (1) Age dating of the first structures that formed within the Milky Way from intermediate-resolution ($\mathcal{R} \approx 2000$), UV/optical (0.34–0.5 μm) spectroscopy of white dwarfs in open and globular clusters.
- (2) Reconstruction of the history of star formation, chemical enrichment and hierarchical merging in Local Group galaxies from intermediate- and high-resolution ($\mathcal{R} \approx 3000, 5000$) optical/near-IR (0.43–0.53 μm , 0.8–0.9 μm) spectroscopy of their halo field stars.
- (3) Mapping of the structure of dark matter halos in elliptical galaxies from high- and intermediate-resolution ($\mathcal{R} \approx 2000, 5000$) near-UV/optical/near-IR (0.36–0.54 μm , 0.6–0.9 μm) spectroscopy for thousands of star clusters and planetary nebulae.
- (4) Tomographic reconstruction of intergalactic medium and an exploration of galaxy-IGM connection at redshifts of $2.5 \lesssim z \lesssim 3$ from low- and high-resolution ($\mathcal{R} \approx 1000, 5000$) near-UV/optical spectroscopy of background Lyman break galaxies across the entire wavelength interval covered by WFOS.
- (5) Measuring the escape fraction of UV photons at a redshift of $z \sim 6$, a key ingredient in understanding the time and duration of the reionization of the universe, from low-resolution ($\mathcal{R} \approx 1000$) optical/near-IR (0.57–0.9 μm) spectroscopy of high- z galaxies.

As described in Section 1.2, these science cases have been chosen partially on the basis of perceived scientific importance, and partially on the basis that they collectively push the requirements of the instrument. Most of these sciences cases have been explored, and optimal observing scenarios devised, with the aid our virtual telescope simulation software. Each subsection is structured along the lines of an observing proposal, with a science justification followed by a technical description. For the sake of descriptive efficiency, calibration steps common to many observing scenarios are described separately in §4.

3.1 Stellar Evolution and White Dwarfs

3.1.1 Background

Photometric and spectroscopic studies of Galactic star clusters have served as the observational foundation for our understanding of stellar evolution, structure, and star formation. The cospatial and coeval characteristics of these resolved stellar populations make them ideal astrophysical laboratories for such studies. Open clusters are valuable as they span wide ranges of age, metallicity, and location from the Galactic center; their older and more massive counterparts, the globular clusters, are equally important as they provide fundamental estimates for the age of our Galaxy, and with a

mild extrapolation, the universe. These ages have typically been measured by comparing theoretical models to the morphology of the main sequence and turnoff in cluster color-magnitude diagrams (CMDs). However, such comparisons are difficult given the many degeneracies and uncertainties in the theoretical isochrones (e.g., the age-metallicity degeneracy). D’Antona (2001) examines this and various other uncertainties in the models (e.g., color-transformations, diffusion processes, sedimentation of heavy elements, convective efficiency, and overshooting) as well as distance uncertainties and concludes that the absolute age of any Galactic globular cluster is only known to within ± 3 Gyrs accuracy (see also Krauss and Chaboyer 2003).

Having been amongst the first objects to form in our Galaxy, all stars in Galactic globular clusters with masses $\gtrsim 0.8 M_{\odot}$ have by now extinguished their nuclear fuel and are therefore no longer on the cluster main sequence. Devoid of any remaining energy sources, the cores of these stars have cooled over billions of years producing a large population of white dwarfs within these clusters. Recently, very deep observations with the Hubble Space Telescope (HST) have unveiled hundreds of these stellar cinders in several of the nearest globular star clusters, such as NGC 6397 (Richer et al. 2005), M4 (Hansen et al. 2004; see also Figure 4), and ω Centauri (Monelli et al. 2005). Although preliminary age estimates can be derived from modelling the luminosity function of white dwarfs in these systems (Hansen et al. 2002; 2004), the key missing ingredient to calibrate the age measurement is a determination of the masses of the white dwarfs along the cooling sequence. In fact, no direct measurement of the mass of a Population II white dwarf has ever been made (i.e., through the fitting of spectral models to observed hydrogen Balmer line profiles).

Equally important to measuring the masses of white dwarfs in globular clusters are mass determination of white dwarfs in open clusters. Open clusters range in age from a few tens of Myrs to 10 Gyrs. Therefore, young clusters still contain very massive main-sequence stars whereas old clusters are nearly as evolved as the globular clusters. Consequently, the white dwarf populations in open clusters vary drastically from one system to another. By measuring the masses of these stars in a sample of clusters of different ages, we can directly constrain fundamental stellar evolution, such as the initial-to-final mass relationship (Kalirai et al. 2005a). This relation connects the mass of the final products of stellar evolution, white dwarfs, to their progenitor mass. It is a required input for constraining chemical evolution in galaxies, determining supernova rates (van den Bergh & Tammann 1991), understanding feedback processes and star formation in galaxies (e.g., Somerville & Primack 1999), and determining distances and ages of globular clusters from modelling their white dwarf cooling sequences (Hansen et al. 2004). Yet, despite its fundamental importance, this relation remains poorly constrained observationally due to the difficulties involved in spectroscopically observing faint white dwarfs (see Weidemann 2000).

3.1.2 Specific science goals

The combination of 1) a 30-meter telescope, 2) a wide-field multi-object optical spectrograph, and 3) CCDs with the high sensitivity in the blue present us with the first opportunity to measure the temperatures, gravities, cooling ages, and masses of faint white dwarfs in star clusters. These observations will accomplish several scientific

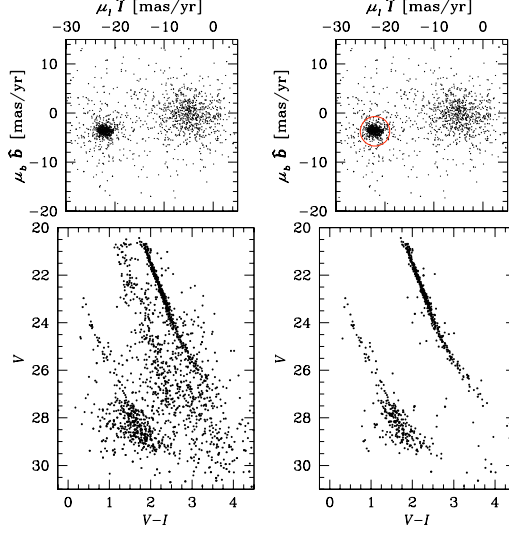


Figure 4: *Left* - The proper motion (top) and color-magnitude diagram (bottom) are shown for all stars detected in a 123 orbit *HST* exposure of the globular cluster M4. The proper motions have been measured by observing the cluster at two different epochs, separated by 6 years. The photometry shows a very tightly constrained M4 main-sequence down to very low main-sequence masses ($0.09 M_{\odot}$) as well as a rich white dwarf cooling sequence. Galactic disk and bulge stars along the line of sight are also seen. *Right* - Isolating just the cluster stars in the proper-motion diagram (top), gives a very clean color-magnitude diagram (bottom) showing a rich white dwarf cooling sequence.

goals:

1. Calibrate the white dwarf cooling sequences in globular clusters and provide us with an entirely independent method for determining the ages of the first structures to form in our Galaxy. The method offers several advantages over canonical techniques for determining these ages. For example, the age-metallicity relation is removed in white dwarfs (all metals have sunk due to the high gravities) and therefore the age spread among the Galactic globular cluster system can be investigated in an unbiased way.
2. Measuring masses of faint white dwarfs in open clusters will dramatically improve our knowledge of how to connect the mass of white dwarfs to the mass of their progenitor hydrogen burning stars, which is of fundamental importance for our understanding of stellar evolution and for many important astrophysical problems.
3. The combination of having an accurate initial-to-final mass relationship and the age of a globular cluster provides us with an excellent probe of the now evolved upper main sequence of a Population II system. The masses of white dwarfs in

globular clusters can be used to determine the progenitor initial mass function of the system (given a good initial-to-final mass relationship).

4. The spectral classification of these WDs will yield important insights into the physics that determines whether white dwarfs are DA (H-rich) or DB (He-rich). Recently, Kalirai et al. (2005b) have found that all massive WDs in star clusters are DA type, a discovery that requires additional data for confirmation.

3.1.3 Observations and Targets

Direct mass measurements of white dwarfs require moderate/high signal-to-noise spectra in the blue. Specifically, the shapes of the highest order hydrogen Balmer lines (H7 at 3970Å [H ϵ], H8 at 3889Å, H9 at 3835Å, etc.¹) are very sensitive to changes in the temperature and gravity of the star (Bergeron, Saffer, & Liebert 1992). Therefore, this program is ideally suited for a large-aperture telescope with blue-sensitive CCDs.

White Dwarfs in Globular Clusters

The nearby Galactic globular star clusters M4 and NGC 6397 are ideal targets for this study. These clusters are nearby (~ 2200 pc) and large (angular diameters of ~ 30 arcmin) and have both been imaged many times, including multiple ultra-deep *HST* observations, and very rich white dwarf populations have already been photometrically identified within them. Figure 4 (bottom-right) shows that within a single *HST* WFPC2 field (≈ 5.5 arcmin²), M4 contains ~ 30 white dwarfs with $V < 26$. With the increased field of view of TMT/WFOS (four $4.5' \times 4.5'$ barrels), we will observe at least 350 white dwarfs to this limit in this cluster, per pointing. A similar number of white dwarfs are also seen in a preliminary CMD for NGC 6397, for which ultra-deep *HST* observations are also available. These clusters have been specifically targeted by *HST* due to their different environments. For example, NGC 6397 is much more metal-poor than M4 ($[\text{Fe}/\text{H}] = -2.0$ vs -1.3) and has a collapsed core². TMT/WFOS will allow us to directly test if NGC 6397 is older than M4 by comparing both the masses of white dwarfs on the cooling sequence (progenitor ages and masses would vary) and by comparing the observed white dwarf luminosity functions in a relative sense. Current generation telescope/instrument combinations (e.g., Keck/LRIS) are unable to reach these scientific goals as reliable mass measurements are limited to white dwarfs with $V < 24$. At this bright limit, very few white dwarfs are present on the observed globular cluster cooling sequences (and they would have no appreciable mass difference).

¹See <http://chinadoll.as.arizona.edu/~schmidt/spol/features.html> for a convenient list which focuses on lines with obvious relevance to astronomy. See http://physics.nist.gov/cgi-bin/AtData/main_asd for a more comprehensive list.

²For readers without a background in astronomy: the bracket notation in this section is a convenient shorthand commonly used to compare the abundance ratios of chemical elements to the corresponding ratios in the sun. $[A/B]$ is defined as the base-10 logarithmic ratio of the chemical abundance of A to B relative to ratio in the sun, *i.e.* $[\text{Fe}/\text{H}] = \log_{10}(\text{Fe}/\text{H}) - \log_{10}(\text{Fe}/\text{H})_{\odot}$. For example, $[\text{Fe}/\text{H}] = -2.0$ means that the ratio of iron to hydrogen is 1% of that in the sun.

White Dwarfs in Open Clusters

In Figure 5 we present a picture of stellar evolution in the form of CMDs for six rich open star clusters in the Canada-France-Hawaii Telescope (CFHT) Open Star Cluster Survey (Kalirai et al. 2001a). The clusters are arranged in order of decreasing age, from NGC 6791 (10 Gyrs) to NGC 2323 (100 Myrs). The clusters show very tight main-sequences, turnoffs, sub giant branches, red giant clumps, and red giant branches. Additionally, a large population of potential white dwarf targets can be seen in the faint blue end of the CMD for each cluster (larger filled points). For many of the older clusters, the photometry is not deep enough to detect all of the white dwarfs. Imaging these systems with TMT/WFOS will easily extend these CMDs to faint enough magnitudes to detect the entire white dwarf population for each of these clusters. This therefore allows the detailed modelling of the white dwarf luminosity functions and yields independent ages for these systems. Follow up TMT/WFOS spectroscopy will provide accurate mass measurements for these white dwarfs. Since the clusters vary in turnoff mass from $\sim 1\text{--}6 M_{\odot}$, the initial-final mass relationship can be developed over a wide progenitor mass range (see Kalirai et al. 2005a for details), thereby constraining the amount of mass that stars lose through their evolution.

3.1.4 Pre-imaging

We will require pre-imaging for all of our targets at least 3–4 weeks before the spectroscopy is scheduled. For the two globular clusters, preimaging is necessary to increase target selection over a larger area than we currently have (one WFPC2 field for M4 and one ACS field for NGC 6397). For the open cluster project, our *CFHT* data cover a large field of view ($42' \times 28'$), however, the photometry is not deep enough to measure the faintest white dwarfs in the older clusters (NGC 6791, NGC 6819, NGC 7789, and M67 – not shown). Pointing locations for these clusters will be chosen by maximizing the density of white dwarfs detected in the *CFHT* data.

The largest contamination in the faint-blue end of the CMD comes from faint galaxies. Adaptive optics is desirable as it would greatly help discriminate white dwarfs from galaxies using morphology criteria. We will eliminate unresolved galaxies by measuring their colors and plotting these on a two-color diagram, $U - B$ vs. $B - V$ or $g - r$ vs. $r - i$. Photometry in such broad band filters is also advantageous as it allows us to fit white dwarf cooling models to the observed white dwarf cooling sequence on the cluster CMDs.

Since only the highest S/N spectra will be fit to models, it is not necessary to obtain ultra-deep imaging. We set our limit at $V = 27$, one magnitude below the faintest targets for which we will obtain a spectrum. Therefore, the imaging aspect of this program represents a small cost of the overall project.

3.1.5 Technical Remarks and Mask Design

Multiobject spectroscopic masks will be constructed in each field using the astrometry from the preimaging. The relevant spectral region in order to determine white dwarf parameters from hydrogen Balmer line spectroscopy is 3700–5000Å (H10 to H β).

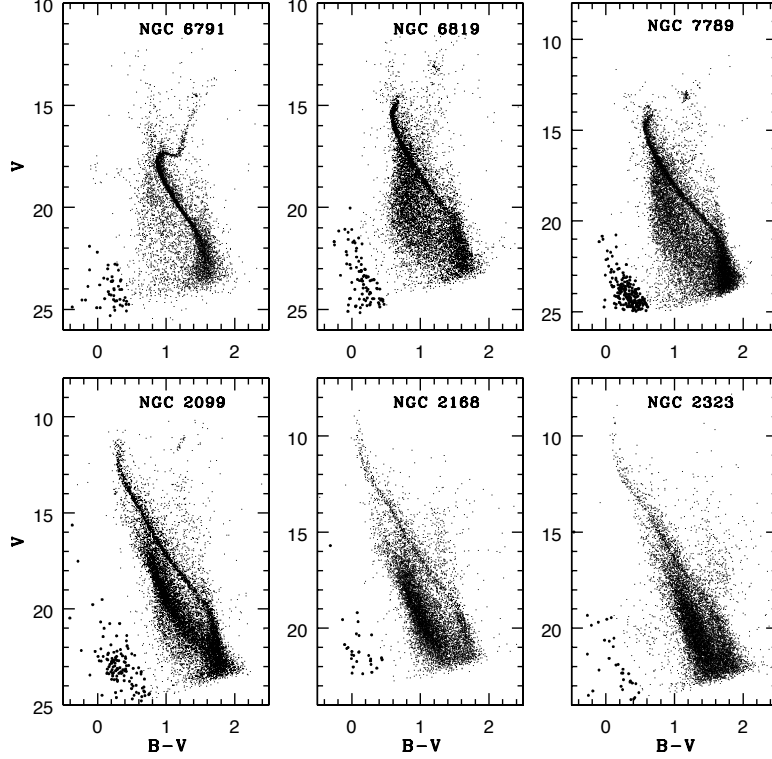


Figure 5: Six rich open star clusters, all observed as a part of the CFHT Open Star Cluster Survey, are shown in order of decreasing age. The oldest, NGC 6791 is 10 Gyrs old whereas the youngest, NGC 2323, is only 100 Myrs old. Rich WD populations in each cluster are highlighted with darker symbols. These stars will all be spectroscopically targeted in future observations to constrain the initial-final mass relationship for different mass ranges.

However, extending this spectral coverage to even bluer wavelengths (i.e., down to the atmospheric cutoff) is desirable in order to determine temperatures of the hotter white dwarfs independently from continuum fitting. This will be especially valuable in other white dwarf related studies with TMT/WFOS. A low resolution ($\mathcal{R} \sim 2000$) grating with the above spectral coverage will be necessary for this project. Additionally, we strongly recommend that a blocking filter be available to restrict the wavelength range to remove the red light. This will allow us to multiplex the observations and increase the density of targets on each spectroscopic mask. We also recommend the use of an atmospheric dispersion corrector to minimize slit light losses. We will set exposure times depending on several factors although we anticipate spending at least half a night on each cluster to maximize the S/N. Masks will be prepared for multiple slit widths to accommodate seeing variations. Although not necessary for this project, overall overhead will be greatly reduced if the mask making process could accept astrometry from other telescopes.

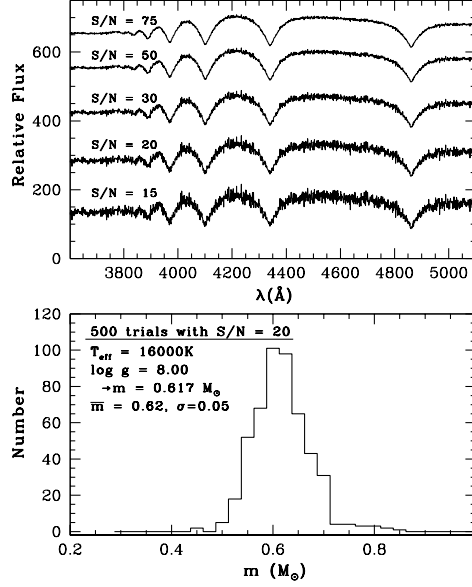


Figure 6: *Top* - Simulated spectra of various S/N are shown. *Bottom* A 500 trial simulation of a WD with S/N = 20. The mean output mass is found to be $M = 0.62 M_{\odot}$ with a dispersion of $0.05 M_{\odot}$ for an input mass of $0.617 M_{\odot}$. This will be the quality of the worst spectra that we obtain in this project. The uncertainty in the mass for brighter stars will be much less.

In Figure 6 (top) we simulate spectra (P. Bergeron et al. 2004, private communication) of white dwarfs with various S/N assuming roughly the configuration above. Only a portion of the spectra are shown for clarity (H8 to H β). In the bottom panel, we present results from fitting white dwarf models to 500 simulated spectra with S/N = 20 (shown as the fourth spectrum in the top panel). At this S/N, we find that we will be able to accurately determine the mass of a white dwarf to within $0.05 M_{\odot}$. We expect this to be the quality of the worst spectrum that we obtain in this project.

In Figure 7 we present real spectra of white dwarfs obtained with Keck/LRIS in the Galactic open cluster NGC 2099 (see Kalirai et al. 2001b). In just 2 hours, we are able to obtain S/N = 15–20 spectra of $V = 23.7$ magnitude stars. Considering the larger aperture and increase in exposure time (0.5–1 night per target), this suggests that we can conservatively set $V = 26$ as our magnitude limit for the spectroscopic program. This limit is faint enough that we will be able to measure masses of white dwarfs at the end of the cooling sequence in all of our open clusters, except NGC 6791 (see Bedin et al. 2005). For this old open cluster, and for the globular clusters, we will constrain masses several magnitudes below the tip of the white dwarf cooling sequence. Those masses will then be used to calibrate the lower cooling sequence given the cluster mass function.

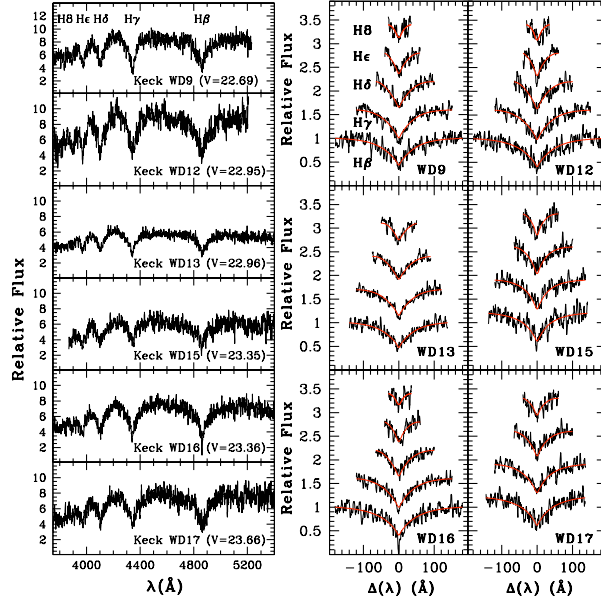


Figure 7: *Left* - Examples of six faint white dwarf spectra are shown ranging from $V \sim 22.7$ to $V \sim 23.7$ (all from Keck/LRIS NGC 2099 data - 2 hours of exp. time). *Right* - The spectral fits of these stars to Balmer line absorption models (Bergeron, Wesemael, & Beauchamp, 1995) is shown. For WD9, we indicate H β , H γ , H δ , H ϵ , and H8. See Kalirai et al. (2005a) for more information.

3.1.6 Path to Science

We anticipate that no other data will be required to complete the goals of this project. White dwarf cooling models can be directly used to age date the globular clusters by comparing the distribution of white dwarfs along the cooling sequence via a luminosity or color function (or both), once the masses of the stars are known. By doing this in two clusters such as M4 and NGC 6397, a relative comparison of the ages yields powerful constraints on the formation timescales of the Galactic globular cluster population.

For the open clusters, we will define the initial-final mass relationship by using the masses of the white dwarfs to first constrain their cooling ages, i.e., the time that each of these stars has spent traversing from the tip of the asymptotic giant branch down to its present white dwarf luminosity. The progenitor main-sequence lifetime is simply the difference between this age and the cluster age. Main-sequence models then yield the initial mass of the progenitor star, and hence a relation between the hydrogen burning mass of a star and its final remnant white dwarf mass.

These observations will also test our finding in Kalirai et al. (2005b) that all open star cluster white dwarfs are DA (H-rich) spectral type (a total sample of some 60 objects, 30% of which come from our NGC 2099 Keck/LRIS study). Based on field white dwarf ratios for the same temperature range from the Sloan Digital Sky Survey (Kleinman et al. 2004), we expect 13 of these stars to be DB (He) spectral type. As

discussed in Kalirai et al. (2005b), we believe this is due to the higher than average mass of the open cluster white dwarf sample (which reduces the subsurface convection zone and prevents the mixing of the surface hydrogen layer into the helium layers below). The older clusters in this study are expected to yield white dwarfs that are much closer in mass to field white dwarfs, and therefore the DA/DB ratio should be restored. These would therefore represent the first DB white dwarfs ever discovered in a star cluster and provide important insights into understanding the chemical evolution of white dwarfs (Bergeron, Ruiz & Leggett 1997).

3.2 Resolved Stellar Populations in the Local Group

3.2.1 Background

Over the last decade or so, individual red giant branch (RGB) stars in distant Local Group galaxies, including the Andromeda spiral galaxy (M31) and its dwarf satellites, have been targeted for moderate- to high-resolution ($\mathcal{R} \lesssim 8000$) spectroscopy with multi-object spectrographs on 8m-class telescopes. At the distance of M31, $d \approx 800$ kpc, the brightest RGB stars have apparent magnitudes in the range $20 \lesssim I \lesssim 22$ and are thus within reach of current large telescopes and their spectrographs: e.g., DEIMOS, LRIS, and ESI on Keck, FORS on VLT, and IMACS on the Magellan telescope (Côté, Oke & Cohen 1999; Reitzel & Guhathakurta 2002; Reitzel et al. 2004; Ibata et al. 2004; Guhathakurta et al. 2005ab). Spectroscopy of RGB stars in Local Group galaxies has allowed astronomers to broadly characterize the halo dynamics of the parent galaxies and to place rough constraints on their chemical abundance distribution. For years to come, observations of this sort will continue to offer our best hope of reconstructing the history of past mergers, star formation and chemical enrichment in the local universe. However, further progress in these key areas is now becoming limited by the light-collecting power of existing telescopes.

The brightest RGB stars have relatively low effective temperatures so it makes sense that the spectroscopy to date has tended to be carried out in the $0.6 - 0.9\mu\text{m}$ wavelength range. The near infrared Ca II absorption triplet feature at $\sim 0.85\mu\text{m}$ is the most prominent spectral features for cool stars in this wavelength range. In most spectroscopic experiments, one can trade off spectral resolution for signal-to-noise. Such a trade-off is not possible in the Ca II triplet region: the veritable “forest” of bright telluric emission lines would render the spectrum useless at low resolution. The path to progress for such projects involves improving the signal-to-noise ratio at a fixed (high) spectral resolution by increasing the light collecting area of the telescope. Thus, TMT and WFOS will allow a giant leap forward compared to present-day telescopes and instruments.

Current hierarchical structure formation models predict that the halos of large galaxies are assembled via the merging/accretion of small stellar subsystems over a substantial fraction of the Hubble time (e.g., Bullock, Kravtsov, & Weinberg 2001; Bullock & Johnston 2005; Font, Johnston & Bullock 2005). There is unmistakable evidence for the ongoing tidal disruption of dwarf satellite galaxies in both the Milky Way and M31 (see, e.g., Ferguson et al. 2002). While our internal perspective makes it difficult to study the structure within our own Galaxy, M31 is ideal because: (1) we have a global external view; (2) its disk is close to edge-on; and (3) it is close enough for us to study individual stars in detail. Wide-field photometric and spectroscopic studies have revealed a substantial amount of substructure in the region within ~ 30 kpc of M31’s center (Ferguson et al. 2002), including a giant tidal stream whose progenitor remains unknown (Ibata et al. 2004; Guhathakurta et al. 2005b), and the existence of a stellar halo extending out to a projected radius of ~ 150 kpc (Guhathakurta et al. 2005a). A detailed characterization of the dynamics and metallicity of these substructures will provide key tests of structure formation theories on sub-galactic scales. Indeed, state-of-the-art numerical simulations of halo assembly predict a wealth of kinematic and

chemical substructure within the halos of massive galaxies such M31, but extracting the history of mergers, star formation and chemical enrichment will likely require spectroscopy for many thousands of RGB stars (see also Figure 8).

3.2.2 Planning of observations

At present, spectroscopic observations are limited by the fact that even long exposures on the largest telescopes and most efficient spectrographs (e.g., Keck+DEIMOS) can only reach only about two magnitudes below the tip of the RGB population in M31, to $I \sim 22.5$. By maintaining a throughput of $\geq 30\%$ over the $0.34 - 1.0\mu m$ region, TMT and WFOS will be able to reach ~ 2.5 mag deeper in the same exposure time, reaching down to the level of the horizontal branch (HB) and allowing an extensive spectroscopic campaign to study the dynamics and metallicities of stars in the outer halo of M31. The steep rise in the RGB luminosity function to faint magnitudes, and the presence of a well-populated HB, means that the surface density of possible targets will be at least ten times higher than is available at present. Figure 9 shows CMDs for three halo fields based on VI imaging from Keck+LRIS. For these particular field locations — at projected distances of $\approx 2^\circ \approx 27$ kpc from the center of M31 — the surface density of RGB stars within the reach of 8m-class telescopes is $\Sigma_{\text{RGB}} \sim 10 \text{ arcmin}^{-2}$. By contrast, with a limiting magnitude of $I \sim 25.5$, we expect $\Sigma_{\text{RGB}} \sim 100 \text{ arcmin}^{-2}$ for WFOS, or roughly 10,000 accessible RGB stars per WFOS field (see Table 1).

Table 1: RGB Candidates in M31

| I (mag) | $\langle I \rangle$ (mag) | $N(I)^\dagger$ | $\Sigma_{\text{RGB}}(I)$ (arcmin^{-2}) | $N(\leq I)^\dagger$ | $\Sigma_{\text{RGB}}(\leq I)$ (arcmin^{-2}) |
|--------------|------------------------------|----------------|--|---------------------|---|
| 20.5-21.0 | 20.75 | 121 | 1.2 | 121 | 1.2 |
| 21.0-21.5 | 21.25 | 241 | 2.3 | 362 | 3.5 |
| 21.5-22.0 | 21.75 | 269 | 2.6 | 631 | 6.1 |
| 22.0-22.5 | 22.25 | 433 | 4.2 | 1064 | 10.2 |
| 22.5-23.0 | 22.75 | 665 | 6.4 | 1729 | 16.6 |
| 23.0-23.5 | 23.25 | 962 | 9.3 | 2691 | 25.9 |
| 23.5-24.0 | 23.75 | 1209 | 11.6 | 3900 | 37.5 |
| 24.0-24.5 | 24.25 | 1612 | 15.5 | 5512 | 53.0 |
| 24.5-25.0 | 24.75 | 2078 | 20.0 | 7590 | 73.0 |
| 25.0-25.5 | 25.25 | 2630 | 25.3 | 10220 | 98.3 |

† – Number RGB stars per WFOS field, for locations of $(\pm 22, \pm 15)$ kpc along the disk major and minor axes, respectively.

Detailed studies of the elemental abundance patterns in Milky Way stars have taught us a great deal about the star formation history of our Galaxy. With WFOS, we are on the brink of being able to make similar measurements in another large spiral galaxy, M31. But even with the world’s largest optical telescope (Keck 10m), one of the most efficient spectrographs available (DEIMOS), and relative long integration times

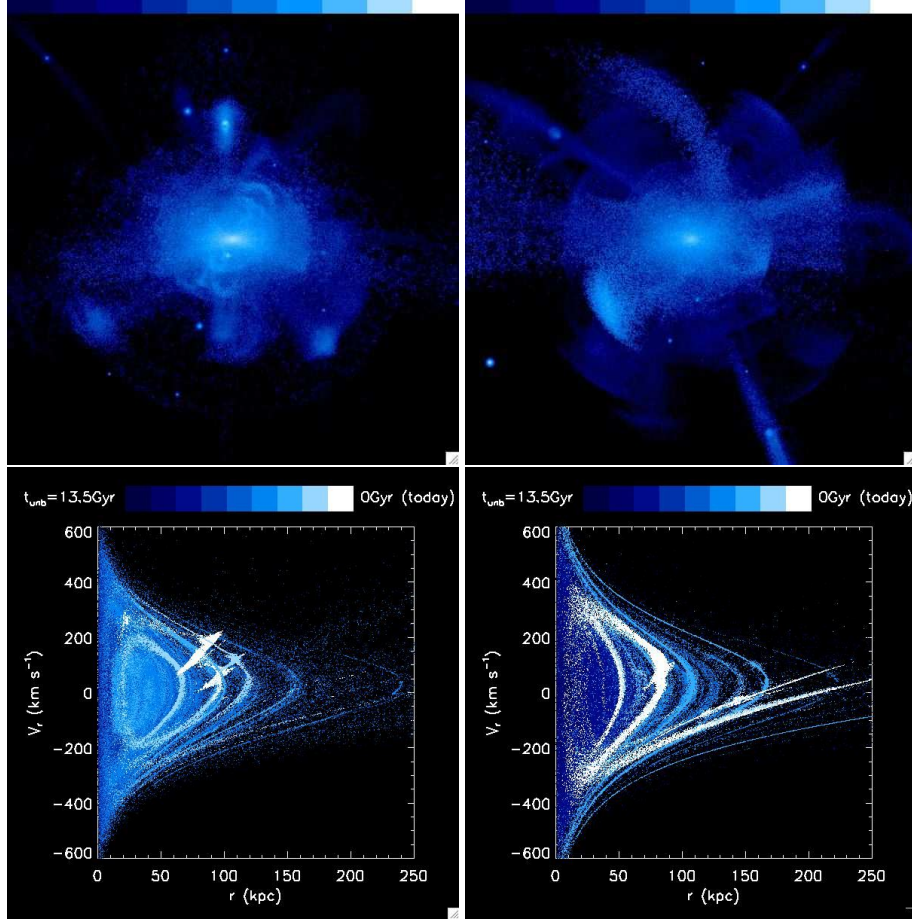


Figure 8: (*Upper Panels*) Two different halo simulations generated using a semi-analytic plus N-body approach. Each box measures 300×300 kpc. The blue/white color scale indicates surface brightness: $23 \text{ mag arcsec}^{-2}$ (white) to $38 \text{ mag arcsec}^{-2}$ (dark blue). (*Lower Panels*) Radial phase space diagrams (v_r vs r relative to the host halo center) for the two halos shown above. Each point represents 1000 solar luminosities. The color code reflects the time each particle became unbound to its parent satellite. White points are either bound or became unbound in the last 1.5 Gyr, while dark blue points became unbound more than 12 Gyr ago. The radial color gradient reflects the tendency for inner halo stars to be accreted (and stripped) early in the galaxy's history. The white feature at $r \sim 80$ kpc in the right panel represents a massive, and very recent, disruption event. Figures and description from Bullock & Johnston (2005).

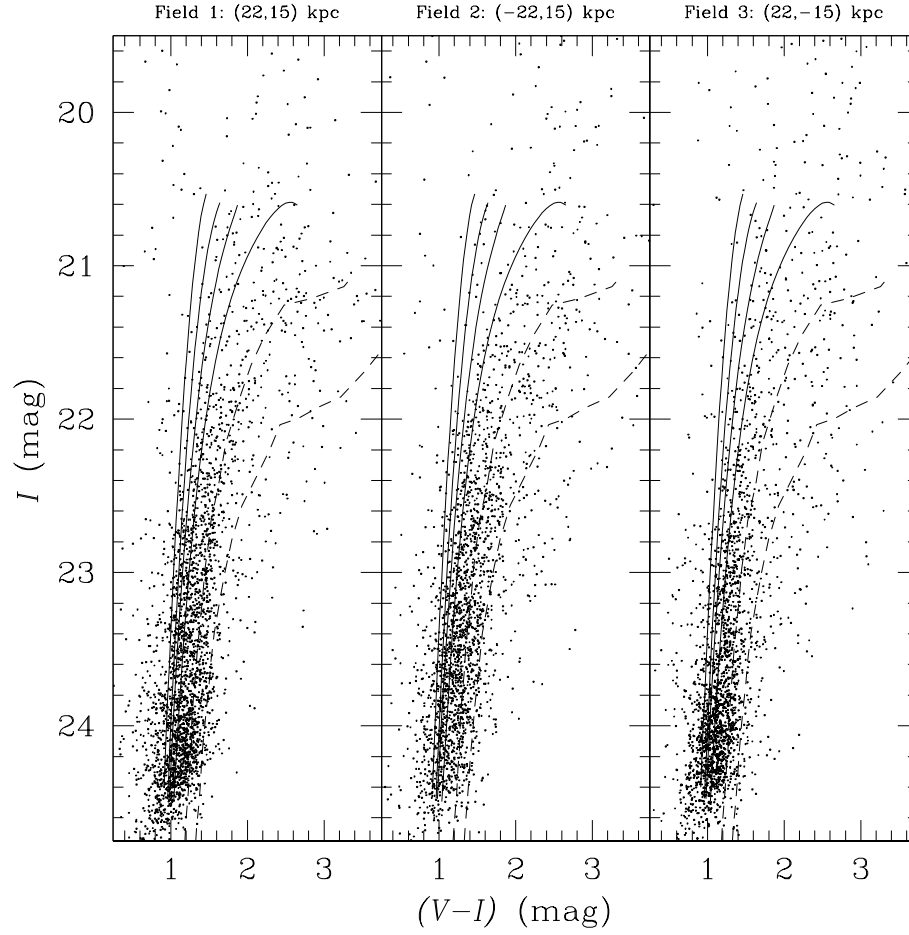


Figure 9: Color magnitude diagrams for three Keck/LRIS fields in the halo of M31. Distances along the major and minor axes are labelled at the top of each panel. The solid curves show fiducial sequences for Galactic globular clusters of metallicity $[\text{Fe}/\text{H}] = -2.12, -1.62, -1.26$ and -0.76 . The dashed curves show 14 Gyr isochrones from Bertelli et al. (1994) with $[\text{Fe}/\text{H}] = -0.4$ and 0.0 . Each of these sightlines contains ≈ 500 RGB stars brighter than $I \sim 22$ within an area of $\sim 80 \text{ arcmin}^2$, the appropriate values for Keck+DEIMOS. TMT+WFOS will reach $I \sim 25.5$, giving a total of 10,000 accessible RGB stars within its $\sim 100 \text{ arcmin}^2$ field of view.

(1–3 hr), it is difficult to achieve signal-to-noise ratios greater than about 15 per \AA for M31’s RGB stars. This S/N is simply not high enough to permit a detailed chemical abundance analysis. In order to improve the S/N ratio, it is necessary to add spectra for RGB stars deemed to be similar based on their location within the CMD. This approach, unfortunately, greatly complicates the interpretation of the spectra because there is no guarantee that the stars had identical physical properties. With TMT+WFOS, this problem will be solved by allowing us to obtain spectra of *individual* RGB stars in M31 with $S/N \gtrsim 40$ per \AA (see Figure 10).

As a demonstration of the scope of Local Group project which WFOS will make possible, we consider an ambitious survey of the M31 halo. The aim of this program is to explore the history of mergers, star formation and chemical enrichment in the M31 halo from radial velocities (accurate to $5\text{--}10 \text{ km s}^{-1}$) for 50,000 RGB stars (covering a 3 deg^2 field) and high-quality abundances for a subset of 10,000 stars (over a 0.9 deg^2 field).

Abundances:

Elemental abundances measurements at a resolution of $\mathcal{R} = 5000$ require a minimum signal-to-noise (S/N) ratio of ~ 40 per \AA . At this resolution, the target S/N ratio is reached (in both the red and blue arms) in exposure times of 3 hours for RGB stars with $I = 21.3$. For a typical halo field, the surface density of RGB stars brighter than this is $\Sigma_{\text{RGB}} \sim 2.6 \text{ arcmin}^{-2}$, or ~ 270 per WFOS field. If a nod and shuffle approach is implemented so that ~ 250 of these stars can be observed during a single setup, then a total of $(10,000/250) \times 3 = 120$ hours (≈ 15 nights) would be required to amass a sample of 10,000 stars. Because the spectra have roughly the same S/N in both arms, it will be possible to measure abundances for both the red and blue spectra. To do so most efficaciously, we target the $0.46 - 0.52 \mu\text{m}$ and $0.8 - 0.9 \mu\text{m}$ spectral regions which contain numerous strong absorption lines. These calculations assume a slit width of $0''.8$ and seeing of $0''.8$ (FWHM) at $0.52 \mu\text{m}$ and $0''.6$ at $0.85 \mu\text{m}$.

Dynamics:

Unlike the chemical abundances portion of the survey, which focusses on long (3 hour) exposures of bright ($I \leq 21.3$) RGB stars, the radial velocity survey targets fainter stars ($I \leq 23$), using shorter exposures (1 hour) to cover a wider area (3 deg^2). While the spectral resolution is unchanged, the primary science goal in this case is the measurement of radial velocities. A signal-to-noise ratio of $S/N \gtrsim 5$ per \AA is adequate to measure velocities good to $\epsilon_v \approx 6 \text{ km s}^{-1}$, which should allow the identification of moving groups, tidal streams and other sub-structures, as well as mass modelling of the dark matter distribution within the M31 halo. The surface density of suitable ($I \leq 23$) RGB stars is $\Sigma_{\text{RGB}} \sim 16.6 \text{ arcmin}^{-2}$, or ~ 1700 per WFOS field. If a nod and shuffle technique can be used to provide a slit length of $4''$ or less, then each 1 hour exposure should yield red and blue spectra for $(380''/4'') \times 4 = 380$ stars per field. Measuring velocities for 40,000 stars (to be added to the 10,000 observed as part of the abundance program) would require $(40,000/380) \times 1 = 105$ hours (≈ 13 nights) assuming that 7 fields could be observed during a typical night. As above, we target the $0.46 - 0.52 \mu\text{m}$ and $0.8 - 0.9 \mu\text{m}$ spectral regions simultaneously. These calculations assume a slit width of $0''.8$ and seeing of $0''.8$ (FWHM) at $0.52 \mu\text{m}$ and $0''.6$ at $0.85 \mu\text{m}$. Both aspects of this program would clearly benefit from GLAO, and might profitably

use even higher spectral resolutions (i.e., $5000 \lesssim \mathcal{R} \lesssim 10000$).

3.2.3 Pre-imaging

Pre-imaging should be taken with WFOS only as a last resort: target RGB stars can be identified, and their coordinates measured, using multi-color imaging from 8m-class telescopes. If the targets must be selected from WFOS images, then standard broadband filters (Johnson, SDSS) would be adequate for this purpose.

3.2.4 Mask design

The observations are not time critical, so there is no need to fabricate masks on short timescales. In fact, the pre-imaging should be taken well in advance to ensure that ample time is available for mask design. Since even the faintest RGBs targeted in this program are well within the reach of optical/IR cameras on 8m-class telescopes, it is essential that the mask design software/hardware be flexible enough to use astrometry from other facilities.

3.2.5 Procedures during the day

There are no special requirements, aside from the need to efficiently measure the positions of the reference pinholes and slit positions in several different masks. In some cases, seven or more fields (28 masks) will be observed each night, so it is important that this procedure should take no more than a few minutes per mask.

3.2.6 Procedures during twilight

No special twilight procedures necessary.

3.2.7 Target acquisition

Field acquisition should rely on the usual approach of positioning and aligning each mask with the aid of a half dozen or so bright reference stars. Many stars of suitable brightness should be available in the direction of M31, which has a Galactic latitude of $b_{\text{II}} \approx -22^\circ$.

3.2.8 Target science data acquisition

The two components of the survey require roughly equal allocations of observing time: about two weeks each. Thus, one month of observing time is needed to observe the full sample of 50,000 RGB stars, distributed over the complete 3 deg^2 field, with accurate abundances for a subset of 10,000 of the brightest stars.

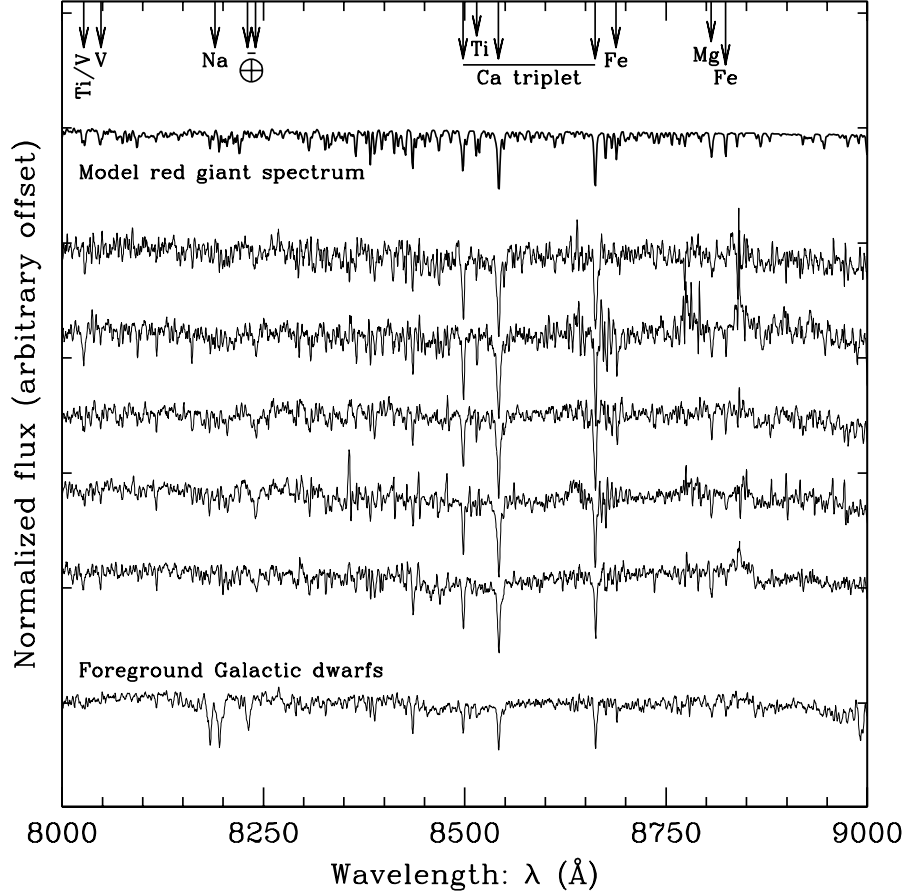


Figure 10: Montage of coadded Keck 10-m/DEIMOS spectra (thin solid lines) showing the region around the Ca II triplet, normalized and shifted to rest-frame wavelength and smoothed with a 1.7\AA weighted boxcar. The bottom spectrum is a coadd of 16 foreground Galactic dwarf stars, each with an exposure time of 1 hr. The next five spectra are coadds of about a dozen M31 RGB stars each, again each with an exposure time of 1 hr, grouped and ordered by predicted Ca II line strength (increasing upward) as estimated from the CMD-based photometric metallicity and luminosity. The bold line at the top is a model red giant spectrum with $T_{\text{eff}} = 4000\text{ K}$, $\log(g) = 1.5$, and $[\text{Fe}/\text{H}] = -0.3$ from Schiavon & Barbuy (1999). A few prominent spectral features of RGB stars are identified along with the $\lambda 8190\text{\AA}$ Na I doublet, which is strong in dwarfs. The S/N in the coadded spectra, typically 50 per \AA , is barely adequate for abundance analysis and the interpretation is complicated by the fact that these are coadded spectra. The TMT+WFOS combination will produce much higher quality spectra for *individual* M31 RGB stars of this apparent magnitude ($I \sim 21$) in 2–3 hour exposures, allowing the determination of elemental abundances (e.g., $[\alpha/\text{Fe}]$ constraints) for many thousands of M31 halo field stars.

3.2.9 Calibration data acquisition

No special calibrations are required, apart from radial velocity standard stars to establish and monitor the zeropoint of the velocities. The portion of the program which requires abundances will require good flux calibration, which may entail observing a few spectrophotometric standard stars.

3.2.10 Facility requirements

No special facility requirement necessary.

3.3 The Dark Matter Distribution in Nearby Elliptical Galaxies

3.3.1 Background

Cosmology has entered a new era, highlighted by recent satellite and balloon missions to study the cosmic microwave background radiation. Boomerang, WMAP, and the upcoming Planck mission, have probed (or will soon probe) temperature fluctuations in the radiation field down to a millionth of a degree or less. The fluctuations observed by WMAP provide a spectacular confirmation of the standard cosmological model, in which a spatially flat, isotropic and homogeneous universe is composed of ordinary matter, dark energy and dark matter.

The existence of this latter component, which may comprise as much as 90% of the mass in the universe, gained widespread acceptance by the astronomical community in the mid 1970s. But despite three decades of study, dark matter remains a mystery. It is detectable only through its gravitational effects, and through gravity it controls the formation of virtually all structures in the universe, from superclusters down to the smallest galaxies. At present, the dominant paradigm for structure formation is the family of cold dark matter (CDM) models, in which the random motions of the dark matter particles are assumed to be much slower than the speed of light. These models provide a remarkably accurate description of the universe on scales larger than ~ 1 Mpc.

However, these same models fail by a wide margin to match observations on the much smaller scales of galaxies. According to the models, the Milky Way should be enveloped in a swarm of several hundred low-mass galaxies, yet exhaustive searches have uncovered only one or two dozen such companions. Equally perplexing, kinematic observations of galaxies suggest that the inner density profiles of their dark matter halos are significantly shallower than the model predictions.

It is unclear if this latter discrepancy represents a failure of the models or limitations in the observations. It is certainly true that attempts to measure dark matter mass profiles for galaxies have produced strongly conflicting results, with claims ranging from dark matter halos that fall steeply with distance from the galaxy center (as expected in CDM models) to dark matter halos with constant-density cores (at odds with the theoretical predictions). But almost all conclusions on the structure of dark matter halos rest on observations of the same *kind* of galaxies: flattened, gas-rich spirals. Very little is known about the dark matter distribution in elliptical galaxies, which are common in the field and which dominate rich galaxy clusters found in the low-redshift universe. The reason is simple: unlike spirals, ellipticals contain little or no cold gas, making the measurement of HI rotation curves impossible. In this section we describe a program designed to measure the distribution of dark matter in nearby elliptical galaxies by determining the radial (i.e., line-of-sight) velocities for dynamical test particles orbiting in their gravitational potential wells. The properties of the dark matter halos can then be studied through their gravitational influence on the motions of the embedded test particles.

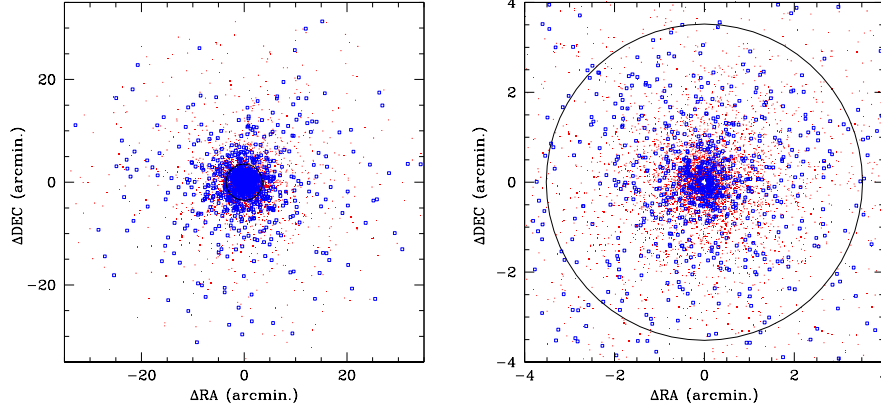


Figure 11: (*Left Panel*) Simulated spatial distribution of ≈ 6000 globular clusters (red points) and ≈ 1100 planetary nebulae (open blue squares) in M49, the brightest elliptical galaxy in the nearby Virgo Cluster. The circle shows the galaxy’s effective radius of $r_e = 3'.5$. (*Right Panel*) A magnified view of the central region of M49. Inside the effective radius (large circle), the mean surface density of globular clusters brighter than $V \approx 25$ is $\langle \Sigma_{GC} \rangle = 90 \text{ arcmin}^{-2}$. The mean surface density for planetary nebulae brighter than $m_{5007} \approx 31$ in this same region is $\langle \Sigma_{PN} \rangle = 16 \text{ arcmin}^{-2}$.

3.3.2 Planning of observations

Reconstruction of the mass distribution in nearby elliptical relies on radial velocity measurements for two independent sets of dynamical test particles: globular clusters (GCs) and planetary nebulae (PNe).

To map out the radial profile of the dark matter mass density, $\rho(r)$, using a system test particles, one must solve simultaneously for the orbital anisotropy of the system of test particles used in the dynamical analysis: $\beta(r) = 1 - \sigma_\theta(r)^2 / \sigma_r(r)^2$.³ This requires a *minimum* sample of ≈ 1000 radial velocities. If one is willing make some assumptions about the orbital distribution (e.g., that the orbits are isotropic, $\beta \equiv 0$), then this requirement can be relaxed to ≈ 250 velocities (Merritt & Tremblay 1993).

At present, radial velocities for ≥ 250 GCs have been amassed for just three elliptical galaxies: M49, M87 and NGC1399 (Côté et al. 2001, 2003; Richtler et al. 2003). These were obvious first targets for multi-object spectrographs on 8m-class telescopes since they are the nearest ellipticals with rich GC systems. But for these same reasons, they constitute a biased sample in terms of luminosity and environment: *i.e.*, they are among the brightest galaxies in the Local supercluster and occupy unique locations in the highest density regions of the Virgo and Fornax Clusters. The situation is even more limited in the case of PNe: in only a single galaxy (NGC5128) does a sample of more than 250 PNe velocities exist (Peng et al. 2004).

The existing observations for these galaxies — along with those for a handful of

³Here $\sigma_\theta(r)$ and $\sigma_r(r)$ are the intrinsic velocity dispersions in the tangential and radial directions relative to the galaxy center.

other galaxies having still smaller radial velocity samples of GCs and PNe — paint a confusing picture about the structure of dark matter halos. Some galaxies appear to be dark matter dominated at their effective radius, r_e , while others seem to show no evidence at all for dark matter out to $r \lesssim 4r_e$ (Napolitano et al. 2005). To elucidate the shape and extent of the dark matter halos in elliptical galaxies, and to examine the dependence of halo properties on galaxy environment, a radial velocity survey of thousands of GCs and PNe in a much expanded sample of galaxies is required.

The table below compares the number of number of elliptical galaxies from the Catalog of Nearby Galaxies (Tully & Fisher 1988) for which radial velocity surveys to a limiting magnitude of $V_{\text{lim}} = 22.7$ would yield minimum radial velocity samples of 250 and 1000 GCs. Note that this is the approximate limiting magnitude for GC radial velocity surveys with 8-10m telescopes. Table 1 shows that, at the present time, samples of this size can be collected for 18 and 4 ellipticals, respectively. With the limiting magnitude of $V_{\text{lim}} \approx 25.5$ expected with WFOS (see below), these samples increase by an order of magnitude: to 179 and 49 galaxies, respectively. Similarly dramatic gains are found for PNe. In short, WFOS opens a realm of study which will never be accessible with multi-object spectrographs on 8-10m class telescopes.

Table 2: Globular Clusters in Elliptical Galaxies

| V_{lim} (mag) | $N_{\text{GC}} \geq 250$ | $N_{\text{GC}} \geq 1000$ | $\langle\sigma_0\rangle$ (km s ⁻¹) |
|---------------------------|--------------------------|---------------------------|---|
| 22.7 | 18 | 4 | 203±34 |
| 25.5 | 179 | 49 | 163±28 |

Note that the final column of Table 1 gives an estimate of the mean projected central velocity dispersion, $\langle\sigma_0\rangle$. This sets the required velocity precision: it is important that the uncertainties on individual velocity measurements, ϵ_v , be no more than $\approx 1/10$ th the system’s intrinsic velocity dispersion, or $\epsilon_v \leq 15\text{-}20 \text{ km s}^{-1}$.

Globular Cluster Observations:

GC systems have a near-Gaussian magnitude distribution, with $M_V \approx -7.4$ and dispersion $\approx 1.4 \text{ mag}$. At the distance of M49, the GC luminosity function “turns over” at $V \approx 23.8$. With limiting magnitudes of $V_{\text{lim}} \approx 22.7$, existing radial velocity surveys with 8m-class telescopes have sampled only a tiny fraction of the GC luminosity function. Figure 11 shows one simulation of the spatial distribution of the ≈ 6000 GCs which belong to this galaxy. The surface density of GCs varies sharply over the field: from $\Sigma_{\text{GC}} \geq 100 \text{ arcmin}^{-2}$ in the galaxy core, to $\Sigma_{\text{GC}} \sim 1 \text{ arcmin}^{-2}$ beyond $10'$. Since most clusters are found within the central $\sim 40 \text{ arcmin}^2$, and because the simultaneous determination of $\rho(r)$ and $\beta(r)$ requires the measurement of the velocity dispersion profile over the largest possible range in galactocentric distance (see the lower left panel of Figure 13), it is important to achieve the highest possible slit densities to maximize survey efficiency.

The best strategy would be to employ a dual approach of: (1) using nod and shuffle to minimize slit length; and: (2) “stacking” the spectra on the detector with the aid of

a band-limiting filter that isolates the spectral region of interest. Since each GC will be observed simultaneously in the blue and red arms, there are two relevant spectral regions: $0.47\text{--}0.54\mu\text{m}$ in the blue, and $0.83\text{--}0.88\mu\text{m}$ in the red. In the blue arm, a resolution of $\mathcal{R} \approx 2000$ will provide adequate velocity precision ($\epsilon_v \approx 20 \text{ km s}^{-1}$ or better) and at the same time allow the measurement of GC ages and metallicities. In the red arm, a higher resolution ($\mathcal{R} \approx 5000$) is required to suppress the noise from bright sky lines in the region of the Ca II triplet.

Table 2 lists some of the spectral lines of interest. While the primary goal of this program is the dynamics of the GC system, such spectra would be valuable probes of the history of star formation and chemical enrichment in the host galaxy. Doing so will require good flux calibration, although this is unimportant for radial velocity measurements.

The upper panel of Figure 12 shows blue spectra for a representative sample of simulated GCs, obtained with WFOS in a single 1 hour exposure. The distribution of velocity errors is shown in the lower panel. For these calculations, the slit width has been matched to the assumed seeing of $\text{FWHM} = 0''.8$.

Table 3: Instrumental Configurations

| Arm | Globular Clusters | | | Planetary Nebulae | | |
|------|-------------------|--|---|-------------------|---|--|
| | \mathcal{R} | λ Coverage ^a (μm) | Diagnostics | \mathcal{R} | λ Coverage (μm) | Diagnostics |
| Blue | 2000 | 0.47–0.54 | Mg I 5167, 5172, 5183 H β 4861 | 2000 | 0.36–0.51 | [O III] 5007, 4959 [O II] 3727 H β 4861, H γ 4342 |
| Red | 5000 | 0.83–0.88 | Ca II 8498, 8542, 8662 | 5000 | 0.58–0.69 | H α 6563 [N II] 6548, 6584 |

^a - Prefilters used to double the effective slit density.

Planetary Nebula Observations:

At the distance of M49, the PN luminosity function shows an abrupt onset at $m_{5007} \approx 26.6$ and rises sharply to fainter magnitudes⁴. Since the distribution of PNe follows the brightness profile of the underlying galaxy, the surface density of sources varies significantly with radius. For sources brighter than $m_{5007} \approx 31$ — the approximate limiting magnitude for WFOS in a single 1 hour exposure — the mean surface density is $\Sigma_{\text{PN}} \sim 16 \text{ arcmin}^{-2}$ within the galaxy’s effective radius ($r_e = 3''.5$). As with the GCs, a “nod and shuffle” technique is required to maximize slit density and boost observing efficiency.

The PNe observations would be carried out simultaneously with the WFOS blue and red arms, using the $\mathcal{R} \approx 2000$ and 5000 gratings, respectively. Table 3 summarizes the important spectral features. With this instrumental configuration, the PNe spectra will contain enough lines to discriminate unambiguously between bonafide PNe and background Ly α galaxies, which are the most severe contaminant in PNe samples. (This would be done by requiring the simultaneous detection of [O III] and H α in the blue and red arms.) The spectral resolution and large number of emission lines between [O II] 3727Å and [N II] 6548, 6584Å would also allow the measurement of chemical

⁴Note that m_{5007} is the magnitude in a narrow-band filter centered on 5007Å.

abundances for individual PNe, giving a first glimpse into the dependence of stellar orbits on age and metallicity in elliptical galaxies. Note that, unlike the situation with the GCs, no blocking filter is needed for the blue arm since it is important to reach the [O III] 3727 Å line, both to confirm the PNe identification and to measure abundances. For this aspect of the program, good flux calibration is a necessity.

Figure 12 shows representative spectra for three simulated PNe in M49, based on a 1 hour integration with WFOS. For these calculations, the slit width has been matched to the assumed seeing of $\text{FWHM} = 0''.8$. The difference between the input and measured radial velocity is plotted against S/N in the [O III] line in the lower right panel of this figure. As with the GCs, we conclude that $\text{S/N} \geq 1$ is adequate to measure velocities of the required precision for even the faintest objects.

3.3.3 Pre-imaging

PNe are faint, emission-line objects which are identified using an on-band/off-band approach to isolate the [O III] 5007Å line and the adjacent continuum with the aid of narrow-band filters. Due to its wide $f/2$ beam, narrow-band imaging is unlikely to be an option with WFOS (at least not at the time of first light). Hence, all pre-imaging for the PNe observations must be taken beforehand with an 8m-class telescope. While the pre-imaging for the GCs can be done with WFOS itself, this is not a necessity: in other words, it is important to retain the option of using pre-imaging either from WFOS, or from some other telescope/camera combination.

At the distance of Virgo, 95% of the GCs will have apparent magnitudes in the range $20.9 \lesssim V \lesssim 26.5$, and are unresolved in typical ground-based seeing conditions. Thus, confusion with foreground stars or compact background galaxies is obviously an issue which needs considering. At the bright end of the GC luminosity function, stars are the dominant source of contamination; at the faint end, unresolved galaxies are the primary concern. In practice, the contamination is usually negligible near the peak of the GC luminosity function, at least for the bright galaxies. For fainter galaxies, contamination can be important at all magnitudes. Rejecting stars and galaxies can be done in a two-color diagram, and SDSS or Johnson filters would be adequate for this purpose. A wide color baseline is needed to separate effectively the stars and galaxies from the GCs: $(g - r)$ vs. $(r - i)$ or $(u - r)$ vs. $(r - i)$.

3.3.4 Mask design

The observations are not time critical, so there is no need to fabricate masks on timescales of days or hours. In fact, the selection of targets may be non-trivial so the pre-imaging should be taken well in advance to ensure that ample time is available for mask design. The ability to place a large number of slits within each field — and maintain accurate sky subtraction at the same time — is the essential element of this program.

It is important that the mask fabrication process be flexible enough to accept pre-imaging from WFOS or some other facility. This would require accurately mapping the geometric distortion in the focal plane during instrument commissioning; indeed, this will be *essential* for the PNe observations (see §6.3.3). Although the choice of slit

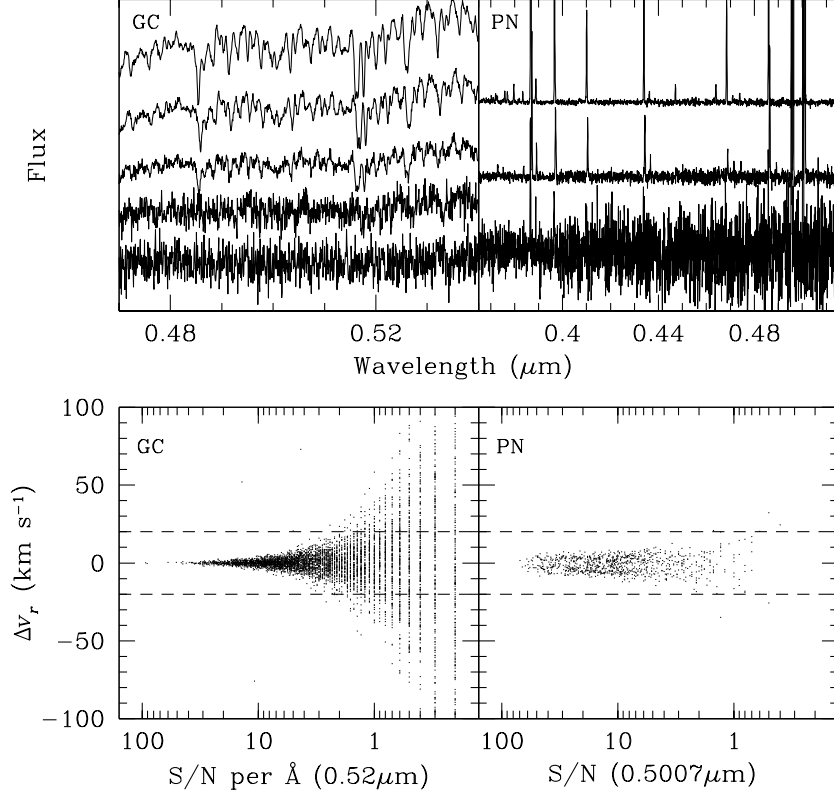


Figure 12: (*Upper Left Panel*) Simulated spectra for five globular clusters in M49, obtained in a 1 hour integration with WFOS ($\mathcal{R} \approx 2000$). The plotted spectra show randomly selected GCs with $V = 19.9$ ($S/N = 43$), 21.5 (25), 22.8 (10.5), 23.6 (2.5) and 25.7 (0.9) where the quoted signal-to-noise ratio refers to the mean per \AA near $0.52\mu\text{m}$. (*Upper Right Panel*) Spectra for three simulated PNe in M49. The spectra have $m_{5007} = 27.0$ ($S/N = 69$), 27.6 (47) and 28.3 (11.5), where the signal-to-noise ratios refer to the central pixel of the [O III] 5007\AA line. (*Lower Left Panel*) Difference between input and measured radial velocity for simulated GCs in M49, plotted as a function of signal-to-noise ratio. The dashed lines show the minimum acceptable velocity error. (*Lower Right Panel*) Difference between input and measured radial velocity plotted against signal-to-noise for simulated PNe. The dashed lines show the minimum acceptable velocity error.

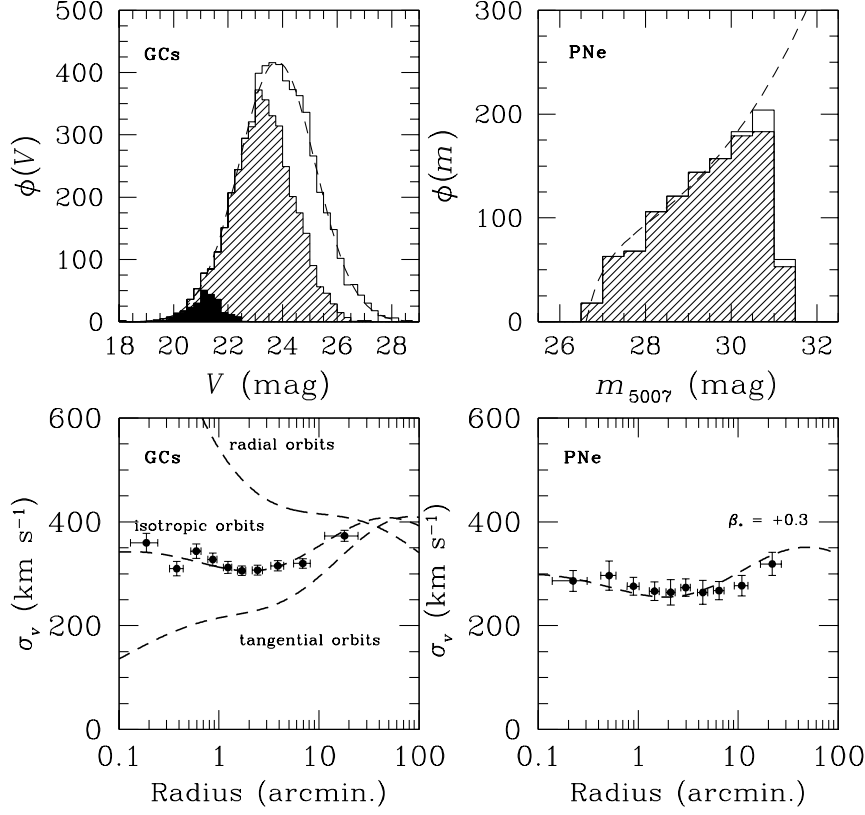


Figure 13: (*Upper Left Panel*) Input luminosity function of GCs belonging to M49 (dashed curve and open histogram). The hatched histogram shows the 4049 GCs for which a 1 hour exposure with WFOS would yield $S/N \geq 1$. The luminosity function of the 263 GCs with existing velocity measurements from Keck is shown as the shaded histogram. (*Upper Right Panel*) Input luminosity function of PNe in M49 (dashed curve and open histogram). The hatched histogram shows the 1065 PNe for which a 1 hour exposure with WFOS would yield $S/N \geq 1$. (*Lower Left Panel*) A simulated measurement of the anisotropy parameter, $\beta \equiv 1 - \sigma_\theta^2/\sigma_r^2$, for the globular cluster system of M49. Different anisotropy parameters are shown by the different curves, from strongly radial ($\beta = +0.99$, upper curve), to strongly tangential ($\beta = -0.99$, lower curve). The measured velocity dispersion profile recovers the assumed isotropic velocity distribution with high confidence. (*Lower Right Panel*) Same as previous panel, except for PNe. In this case, the dashed curve shows the velocity dispersion profile for the assumed (input) case of mildly radial stellar orbits, $\beta_* = +0.3$.

width will depend on the observing conditions and the requisite velocity precision, it will normally fall in the range $0'.4\text{--}0'.8$.

Due to the high surface densities of GCs in the inner regions of the galaxy (i.e., see Figure 11), it would be advantageous to boost the effective slit density by inserting a blocking filter which restricts the wavelength range to $0.47\text{--}0.54\mu\text{m}$, thereby doubling the effective slit density. Depending on the cosmic-ray rate, lunar phase and object magnitude, total exposure times may be as short as ≈ 0.5 hour. It is therefore a requirement that as many as ten masks per barrel be available for use on any given night.

3.3.5 Procedures during the day

To minimize field acquisition time, it will be necessary to accurately measure the location of the reference pinholes and slit positions in the various masks. This should be done during the afternoon, after the masks have been loaded, by taking short images of the illuminated masks with no dispersing element in place. Because of the potentially large numbers of masks (ten per barrel, or 40 in total) this procedure should take no more than 3 minutes per mask.

3.3.6 Procedures during twilight

No special twilight procedures necessary.

3.3.7 Target acquisition

A “classical” target acquisition scenario — in which pinholes for 4–7 bright reference stars are imaged through each mask — will be adequate for this program. The Galactic latitude of M49 is $b_{\text{II}} \approx 70^\circ$, so the number of suitable reference stars may be limited. It should be possible to measure the centroids of these stars on the detector to the 1–2 milliarcsecond level in an exposure of $\approx 10\text{s}$. As many as ten masks per barrel may be used in a single night, so the acquisition time should be minimal. This will be a much more important specification for WFOS than for existing spectrographs as it will be necessary to perform target acquisition and mask alignment for as many as four channels simultaneously. Once the telescope has slewed to the target field, the alignment process should take no more than 3 minutes.

3.3.8 Target science data acquisition

The upper panels of Figure 13 show the simulated luminosity functions of GCs and PNe in M49 (open histograms). The hatched histograms show all objects for which a single 1 hour exposure with the blue arm of WFOS would yield $S/N \geq 1$, the minimum needed to ensure a velocity precision of $\epsilon_v = 20 \text{ km s}^{-1}$ or better for both the GCs and PNe (see Figure 12). The lower panels of Figure 13 demonstrate how such large radial velocity samples can be used to measure not only the distribution of dark matter but also the orbital properties, $\beta(r)$, of the different tracer populations.

Measuring velocities for the complete samples of GCs (≈ 4000) and PNe (≈ 1000) in M49 which fall into this category (i.e., $S/N \geq 1$ in 1 hour) would require ~ 12 ,

1-hour exposures for the GCs and ~ 7 , 1-hour exposures for the PNe. This estimate assumes that a “nod and shuffle” technique can be used to achieve accurate sky+galaxy subtraction with slit lengths of $4''$. For the GCs, we further assume that a prefilter isolating the $0.47\text{--}0.54\mu\text{m}$ spectral region can be used to place two banks of spectra on each WFOS channel. Since the total slit length available in each channel of the spectrograph measures $6'.36$, we expect roughly $4 \times 2 \times (380''/4'') = 760$ slits per GC mask, and about half this number for the PNe masks. Multiple pointings inside the galaxy’s effective radius will be needed because of the high surface densities in this region.

If we concentrate for the time being on just the GC aspect of the program, then a sample of $\gtrsim 1000$ velocities for GCs in M49 could be amassed in about 2–3 hours of integration time. From Table 1, we see that about 50 galaxies with suitably rich GC systems are found in the Catalog of Nearby Galaxies. Thus, a comprehensive study of the structure of dark matter halos in these galaxies, based on radial velocity samples of 1000 or more GCs per galaxy, would require a total “open shutter” integration time of $2.5 \text{ hours} \times 50 \approx 125 \text{ hours}$ (≈ 15 nights).

3.3.9 Calibration data acquisition

Since the program uses radial velocities of discrete objects to derive M49’s velocity dispersion and its variation with radius, it is important that zeropoint be stable and easily tied to a standardized reference frame. This is particularly true since velocities derived from masks taken months or years apart will be combined to map out the velocity field. Because the faintest galaxies in Table 1 have (roughly flat) velocity dispersion profiles of $\approx 150 \text{ km s}^{-1}$, we require velocity uncertainties no larger than 15 km s^{-1} . Spectra for radial velocity standard stars should be undertaken each night, perhaps using masks for multiple radial velocity standard stars located in Galactic open or GC fields.

3.3.10 Facility requirements

No special facility requirement necessary.

3.4 Observing Three-Dimensional Baryonic Structure During the Epoch of Galaxy Formation

3.4.1 Background

There have been two very significant developments in understanding the high redshift universe that have emerged in the last decade of 8-10m class telescopes. First, with the advent of high resolution spectrographs on these telescopes (most notably Keck/HIRES and VLT/UVES), quasar absorption line spectroscopy (coupled with increasingly sophisticated numerical simulations of structure formation) has revolutionized our view of the diffuse intergalactic medium. This technique uses distant, albeit luminous, QSOs as background beacons on whose continua the absorption profiles of intervening gas reservoirs are imprinted. The beauty of this approach is that galaxies and other gaseous structures in the IGM are detected independent of their luminosity. Moreover, the information accessible in the absorption line spectra is of extremely high quality, with many orders of magnitude more sensitivity than would be possible if the gas were required to be “self-luminous”. For example, the $\text{Ly}\alpha$ line provides such a sensitive probe of neutral hydrogen gas that densities much less than the cosmic mean can be easily detected at redshifts $1.6 \lesssim z \lesssim 3.5$. Through these kinds of studies, we have learned that diffuse gas in the intergalactic medium is a reliable tracer of the initial dark matter power spectrum on small scales that are not measurable using self-luminous objects (because sites of galaxy formation have become much too non-linear by the observable cosmic epochs). We have also learned that much of the intergalactic gas, if not all of it, has been enriched by an early generation of star formation in galaxies. It is estimated that at $z \sim 3$, $\sim 90\%$ of the baryons in the universe reside in the diffuse intergalactic medium; thus, the IGM acts as both a reservoir for fueling the galaxy formation process, and as a sink for receiving its products (e.g., metals, energy). The main limitation of the IGM studies is that QSOs bright enough to act as background beacons are very rare, and the information content along a single line of sight, while of extremely high quality, does not provide three-dimensional information and does not show directly how the absorption signatures relate to luminous objects inhabiting the same (or nearby) regions of space.

Meanwhile, great progress has been made in our ability to routinely study large numbers of galaxies at similar redshifts, thanks to sensitive multi-object optical spectrometers (e.g. Keck/LRIS, Gemini/GMOS, VLT/FORS) on current generation telescopes. Many of these galaxies have spectra that are quite similar to those of QSOs through the rest-frame far-UV, but they are generally much fainter than the QSOs that have been used for the absorption line spectroscopy discussed above. Samples of such galaxies have allowed us to understand how they are distributed in space, statistically, and have allowed the construction of their luminosity distributions in various observed wavebands. The statistical study of high redshift galaxies has been truly revolutionized in the last decade, and has given us a crude picture of the global star formation history of the universe, at least over the last $\sim 90\%$ of the age of the universe. The relevant cosmological model has been similarly revolutionized over the same period, to the point that many of the most significant unresolved questions in understanding how galaxies form relate to the physics of the baryons (and not the distribution of dark mat-

ter) and how the energy produced by star formation, supernova explosions, and AGN accretion affect the subsequent development of structure on galaxy scales. In short, there is a developing broad-brush picture of *when* galaxy formation is happening, and techniques exist for finding and collecting samples of most of the denizens of the high redshift universe, but we are lacking a detailed physical picture of *how* galaxies form. The answers to the questions related to “gastrophysics” require greater sensitivity and synthesis of techniques, such as we are suggesting below.

A simultaneous study of galaxies and the diffuse intergalactic medium, in the same volumes of space, offers the possibility of combining two powerful lines of investigation that provide complementary information on the state of baryons, both those collapsed into galaxies and those remaining in between the galaxies. The IGM represents a laboratory in which the effects of galaxy formation and AGN accretion (e.g., radiative and hydrodynamical “feedback” and its recent history) can be measured on scales that are not accessible using direct observations of galaxies, and, similarly, the galaxy distribution relative to the lines of sight to background objects tells us more about how the physical information garnered from the absorption line studies should be interpreted.

We are proposing a large survey of the high redshift universe that combines absorption line studies with direct observations of galaxies and active galactic nuclei in the same cosmic volumes. Our current understanding of global star formation in galaxies, and also of the evolution of supermassive black hole accretion as inferred from AGN surveys, suggests that the redshift range $1.8 \lesssim z \lesssim 3.5$ includes the most active period in the universe’s history for both processes. It is also the range over which neutral hydrogen in the IGM can be observed with high dynamic range from the ground using both background QSOs and galaxies, as we discuss.

The limitation on the sampling density of sightlines for absorption line studies is overcome through TMT’s large collecting area, the high spectral throughput of WFOS, and the novel use of background *galaxies* to study HI and metals in the IGM. The surface density on the sky of QSOs of course increases with decreasing brightness, reaching $\sim 100 - 200$ per square degree ($\sim 0.03 \text{ arcmin}^{-2}$). However, as shown in Figure 14, the surface density of UV-bright galaxies is $\sim 100 - 200$ times higher by $R_{AB} \sim 24.5$ (approximately the magnitude at which WFOS can obtain spectral resolution $\mathcal{R} \sim 5000$ and $S/N \geq 30$.) The observed surface density of UV-bright galaxies to that limit of $2\text{-}3 \text{ arcmin}^{-2}$ translates to a proper spatial sampling of a few hundred kpc (with the currently accepted cosmology). Observing the entire grid of background sources (QSOs and galaxies) thus provides for the first time the possibility of the 3-D “tomographic” reconstruction of the IGM, at a spectral resolution that is adequate to resolve the typical thermal width of intergalactic HI clouds and to discern even relatively weak lines of metallic species whose wavelengths appear longward of Lyman α emission in each probe’s rest frame. The galaxy spectra thus obtained will also allow unprecedentedly detailed spectra of the galaxies, containing information on the chemistry, kinematics, and stellar populations which are currently possible only for rare strongly-gravitationally lensed objects (see, e.g., Pettini et al 2002).

3.4.2 Specific science goals

Our goal is to execute a WFOS program to survey the IGM–galaxy system over a volume of the $1.8 < z < 3.5$ universe that is as statistically representative as the Sloan Digital Sky Survey (SDSS) at $z \sim 0.1$. The SDSS field of view (2.5 degrees in diameter) equates to a transverse scale of ~ 18 Mpc at the survey’s median redshift; the same co-moving scale at $z \sim 2.5$ subtends only 10.6 arcmin. By the same token, WFOS can survey the 10^8 Mpc^3 achieved by the SDSS in a solid angle of only 5 square degrees. This would most sensibly be done in at least 4 separate survey fields of $\sim 1.25 \text{ deg}^2$ each, well separated in RA but at declinations allowing for long integrations on a given night (i.e., depending on the latitude of the observatory).

The WFOS galaxy/IGM tomography project consists of two components. The first component is to obtain high S/N (~ 30), $\mathcal{R} \sim 5000$ spectra of objects (QSOs, AGN, and galaxies) with $R < 24.5$. Over the 5 square degree survey area, we expect $\sim 40,000$ such objects which will be used as background sources to trace intervening absorption and as high quality spectra for the evaluation of detailed galaxy properties. We can reasonably hope to observe $\sim 80\%$ of these, as discussed below. We will also obtain lower resolution ($\mathcal{R} \sim 1000$) spectra of fainter galaxies ($24.5 < R < 26.5$), of which there will be a total of $\sim 2.5 \times 10^5$ in the redshift range of interest, of which we would hope to observe $\sim 2 \times 10^5$. The survey would simultaneously yield a very detailed map of large scale structure, and the quasi-3D distribution of neutral hydrogen and metals in the diffuse IGM, observations which are impossible at lower redshift and with smaller telescopes. It will allow the measurement of the radiative and hydrodynamic influence of QSOs, AGN, and galaxies on their environments, addressing some of the most crucial remaining questions in understanding galaxy formation, AGN activity, and the nature of the intergalactic medium.

3.4.3 Planning of observations

A key to planning the details of the observations is a good statistical knowledge of the density of targets for each of the two components of the survey. From work completed using 8-10m class telescopes, coupled with very deep imaging surveys, it is well known that simple broad band selection criteria can be used to select star-forming galaxies and AGN in prescribed ranges of redshift, typically with a breadth of the redshift selection function of $\sigma(z) \simeq 0.3 - 0.4$ (e.g., Steidel et al. 2004). Figure 14 shows that, with a combination of two such color-selected galaxy samples, a well-defined range of redshifts matching the cosmic volume targeted in the survey can be assembled, and it allows us to examine issues related to assignment of objects to slit masks and the achievable observing efficiency.

For this science demonstration, we have chosen the field around the QSO HS1700+64 for which wide-field, multi-band photometry already exists, and where significant spectroscopy of the brighter high redshift galaxy candidates satisfying the same selection criteria as the samples in Figure 14 has already been obtained. A single WFOS barrel’s FOV is indicated in Figure 15, superposed on an R -band image of the field which reaches the desired $R = 26.5$ depth (the catalogs of galaxy candidates at the faintest magnitudes are incomplete due primarily to the depth in the other two passbands

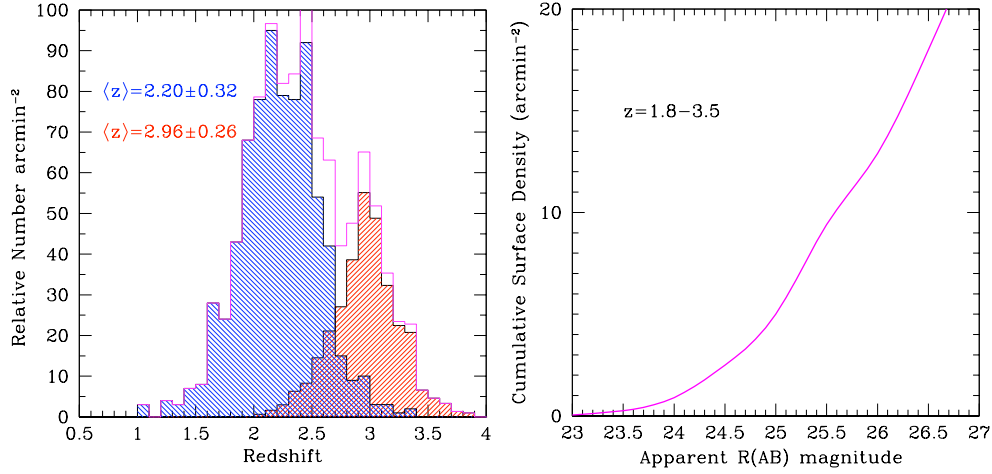


Figure 14: (Left) The relative surface density versus redshift for rest-UV selected galaxy samples to a fixed apparent magnitude limit (based on spectroscopic samples observed to $R(AB) = 25.5$). The relative distribution of objects to $R(AB) = 26.5$ is expected to be similar. The magenta histogram is the sum of the two subsamples. (Right) The cumulative surface density of galaxies in the targeted redshift range $1.8 \lesssim z \lesssim 3.5$ as a function of apparent magnitude, based on measured rest-frame far-UV luminosity functions obtained from existing large spectroscopic samples.

needed to isolate the samples; in practice the required depth is easily achieved even with 4m-class telescopes with long integration times). As can be seen in Figure 14, the surface density of galaxies in the redshift range of interest has reached $\sim 15 \text{ arcmin}^{-2}$ by $R(AB) = 26.5$, so that a typical single barrel of WFOS will contain several hundred candidates for the faint survey and $\sim 70 - 80$ candidates for the $\mathcal{R} = 5000$ survey. The outcome of the mask design in the particular footprint shown in Figure 15 is discussed further below.

It is important to note that target selection based on broad-band colors is rather trivial, and is quite clean in the sense that few objects will lie outside the targeted redshift range(s). It is therefore not essential for any spectroscopy to have been done in the survey fields prior to the TMT/WFOS observing program. However, it may improve the efficiency of mask design either to observe all of the bright candidates first using the $\mathcal{R} = 1000$ configuration described below, or to have measured precise redshifts for the bright sub-sample using 8m class telescopes. Based on experience with long integrations on a 10m telescope, it is not unreasonable to expect 100% spectroscopic completeness for observed galaxies in the suggested integration times.

The nominal resolution required for high quality tomography of the IGM is $\mathcal{R} = 5000$ (see later and in Figure 16 for the impact of this resolution choice). In round numbers, this is the minimum required to resolve typical Lyman α forest H I lines having Doppler parameters $b \sim 30 \text{ km s}^{-1}$, or $\text{FWHM} \sim 50 \text{ km s}^{-1}$, and is also approximately the minimum resolution required for the detection of relatively weak absorption lines of metallic species, most notably CIV $\lambda\lambda 1548, 1550$. There is of

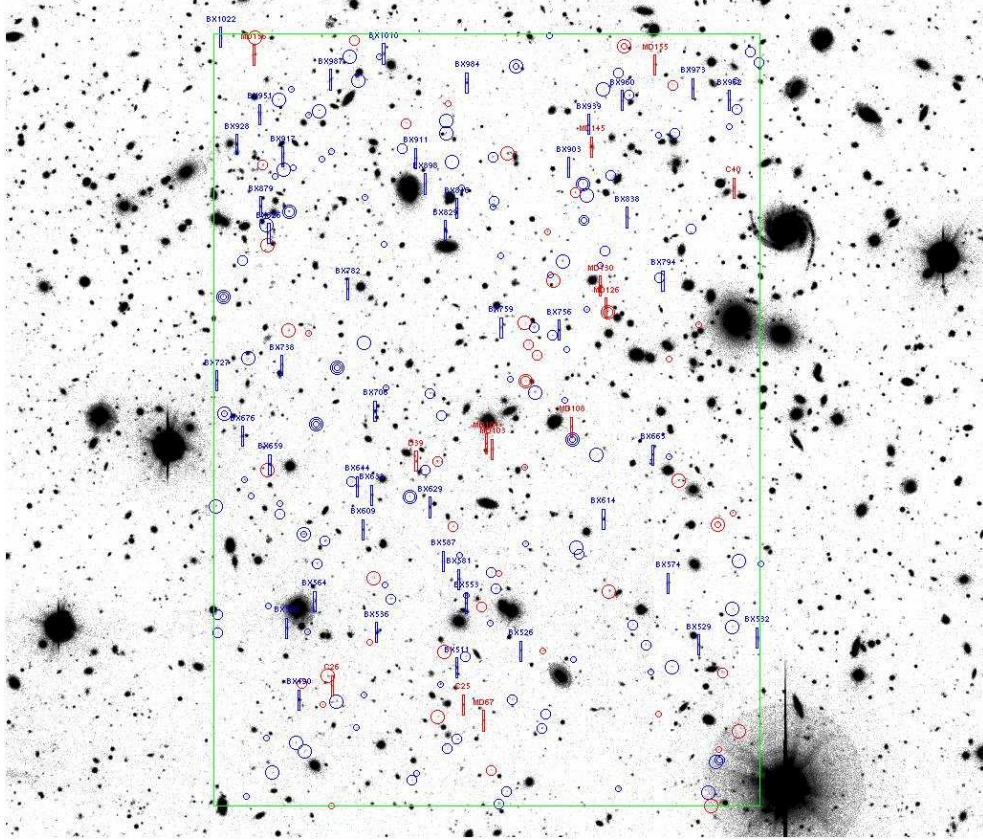


Figure 15: Spectroscopic coverage for a single barrel of WFOS, whose angular size is indicated in green. The image is a deep R-band image of our science demonstration field. In two passes with the $\mathcal{R} = 5000$ configuration, indicated for illustration purposes with 10 arcsec slitlets, 58/70 objects (83%) with $z = 1.8 - 3.5$ and $R \leq 24.5$ are observed, with 19 objects repeated on the second pass. The slit colors are coded as in Figure 14, according to their likely redshifts based on color. For the faint galaxy $\mathcal{R} = 1000$ configuration, 3 passes on the identical footprint places slits on 168/245 candidates (69%), of which 17 objects were observed more than once. These objects are indicated with circles of different sizes for each pass, and are color coded in the same way as the brighter objects.

course a trade-off between spectral coverage in a single observation and the achieved spectral resolution, and indeed interesting characteristics of the IGM can be obtained even with resolution as low as $\mathcal{R} \sim 1000$ (so that even the fainter object portion of the program will yield quantitative results on the IGM on still smaller spatial scales than afforded by the higher quality $\mathcal{R} = 5000$ spectra of the brighter sub-sample).

For the higher resolution configuration, the key wavelength range to be covered is the “Lyman α forest” between Lyman α (1215.7 Å) and Lyman β (1025.7 Å) at the emission redshift of the object. For example, at the expected median redshift of $z_{em} = 2.4$ for the $\mathcal{R} = 5000$ targets, this corresponds to the wavelength interval 3490–4130 Å covering the Lyman α transition over the redshift range $z = 1.87 - 2.40$; the corresponding interval would be 4105–4865, for $z_{em} = 3$, tracing the neutral hydrogen distribution along the line of sight over the redshift range $z = 2.38 - 3.00$. Ideally, the red spectrometer channel would observe the spectral region covering the CIV transition over the same range in redshift as observed for Lyman α in the blue channel, or 4450–5270 Å for the case of $z_{em} = 2.40$ and 5230–6200 Å for $z_{em} = 3.00$.

The baseline detector/camera package for WFOS provides a “dispersion length” for each barrel of 510'' so that at $\mathcal{R} = 5000$ for a 0.7 slit there would be ~ 730 independent resolution elements across the detector. Placing slits at the extreme field positions (± 2.25 arcmin) would shift the wavelength coverage by $\sim \pm 27\%$ of the spectral coverage relative to a slit positioned at the center of a barrel. The situation is summarized for two potential spectrometer configurations in Table 3. Clearly, there is no single configuration that will be optimal over the entire desired redshift ranges. It is possible to extend the wavelength range by $\sim 25\%$ by making the detector package larger, but this does not solve the main problem: the spectral range is limited at such high spectral resolution because of limitations on the camera acceptance angle and f-ratio. The default field layout on the plane of the sky will require partially redundant pointings of the telescope in order to cover a contiguous area of sky; in principle, the same object can be observed more than once with a slit placed at a different X coordinate in the focal plane of a spectrometer barrel, meaning that one could increase the wavelength coverage by as much as $\sim 50\%$ with a second observation of a given object. The surface density of $\mathcal{R} = 5000$ targets is low enough that repeats will happen naturally for a significant fraction of the targets, as detailed below. In addition, if the redshifts of the bright sources are known *a priori*, as may be the case if they have been observed first at $\mathcal{R} = 1000$ or previously with 8-10m class telescopes, one could add a level of complexity to the mask design software (not yet implemented) that would account for the optimal “X” position for a slit assigned to a particular object. [We should also consider halving the spectral resolution to double the wavelength coverage. Much of the science could be done with half the resolution while increasing the overall information content per spectrum].

It will not be practical to fine-tune wavelength ranges for every target to obtain precisely the desired range of wavelengths on each channel, and one will accept whatever range is recorded. It would be a mistake to conclude that wavelength ranges outside of these small windows are not useful for many scientific questions; for example, data obtained at wavelengths shortward of 3650 Å for objects with $z_{em} \simeq 3$ will be able to directly measure the leakage of Lyman continuum radiation from the galaxy (i.e., it would measure the flux of photons with $\lambda_0 < 912$ Å), an extremely challenging

Table 4: $\mathcal{R} = 5000$ Configuration examples, with the baseline detector package

| Blue: $\lambda_c = 3820 \text{ \AA}$; dichroic=4300 \AA | | |
|--|-----------------|-----------------|
| Mask pos. (Δ arcmin) | λ_{min} | λ_{max} |
| 2.25 | 3394 | 3954 |
| 1.50 | 3440 | 4000 |
| 0.00 | 3540 | 4100 |
| -1.50 | 3640 | 4200 |
| -2.25 | 3685 | 4345 |
| Red: $\lambda_c = 4860 \text{ \AA}$; dichroic 4300 \AA | | |
| Mask pos. (Δ arcmin) | λ_{min} | λ_{max} |
| 2.25 | 4315 | 5205 |
| 1.50 | 4380 | 5090 |
| 0.00 | 4505 | 5215 |
| -1.50 | 4630 | 5340 |
| -2.25 | 4695 | 5405 |
| Blue: $\lambda_c = 4500 \text{ \AA}$; dichroic= 5000 \AA | | |
| Mask pos. (Δ arcmin) | λ_{min} | λ_{max} |
| 2.25 | 3995 | 4655 |
| 1.50 | 4053 | 4713 |
| 0.00 | 4170 | 4830 |
| -1.50 | 4287 | 4947 |
| -2.25 | 4345 | 5005 |
| Red: $\lambda_c = 5720 \text{ \AA}$; dichroic=5000 \AA | | |
| Mask pos. (Δ arcmin) | λ_{min} | λ_{max} |
| 2.25 | 5080 | 5920 |
| 1.50 | 5150 | 5990 |
| 0.00 | 5300 | 6140 |
| -1.50 | 5450 | 6290 |
| -2.25 | 5520 | 6360 |

observation at present but one which should be quite routine with TMT/WFOS. Such observations could be used to evaluate the importance of local sources of UV ionizing photons on the physical state of the nearby IGM, one of the many benefits of the simultaneous observation of the IGM and sources of ionizing photons.

We have chosen $\mathcal{R} = 1000$ as the optimal resolution for the faint galaxy portion of the survey for two reasons: (1) the typical intrinsic width of features in the spectra of faint galaxies are $\text{FWHM} \sim 300 - 600 \text{ km s}^{-1}$ (these tend to be interstellar absorption lines widened by the kinematics of outflowing material in galactic superwinds, with weaker lines being narrower) and matching the spectral resolution to the expected line widths provides maximum contrast for features essential to redshift identification; and (2) the resolution is just high enough to resolve the CIV doublet so that at least strong intervening absorption line systems can be identified in many of the galaxy spectra; it is also just high enough that the level of absorption in the Lyman α forest reasonably

Table 5: $\mathcal{R} = 1000$ Configuration Examples

| Blue: $\lambda_c = 4650 \text{ \AA}$; dichroic=5600 \AA | | |
|---|-----------------|-----------------|
| Mask pos. (Δ arcmin) | λ_{min} | λ_{max} |
| 2.25 | (3200) | 5267 |
| 0.00 | (3200) | (5600) |
| -2.25 | 3730 | (5600) |
| Red: $\lambda_c = 6700 \text{ \AA}$; dichroic 5600 \AA | | |
| Mask pos. (Δ arcmin) | λ_{min} | λ_{max} |
| 2.25 | (5600) | 7840 |
| 0.00 | (5600) | 9075 |
| -2.25 | (5600) | 10310 |

accurately reflects the mean HI opacity in the corresponding segment of the IGM (see, e.g., Adelberger 2004). There is always a temptation to place multiple tiers of slits in the focal plane and avoid overlap of spectra by using lower dispersion, which works well in the limit of very high object surface density on the sky. Our experiment below, even with surface densities of $\gtrsim 10 \text{ arcmin}^{-2}$, suggests that the multiplexing gain would be considerably smaller than a factor of two for two ranks of slits, and the loss of spectral resolution would have a significant scientific cost (not to mention issues related to scattered light, order blocking, etc.).

For the $\mathcal{R} = 1000$ configuration, the number of spectral resolution elements is of course conserved so the spectral coverage would increase by a factor of 5 relative to the $\mathcal{R} = 5000$ case. It will be possible to cover ~ 1 octave in wavelength with a given spectrometer channel, so that a configuration producing a central wavelength of 4650 \AA for a slit at the center of the field would cover $\sim 2930 - 6340$ (i.e., $3200 - \lambda_d$, where λ_d is the dichroic half power point assuming it is shortward of 6340 \AA), so that the useful spectrum would cover $\sim 70\%$ of the detector for the configuration summarized in Table 4, which has the dichroic set at 5600 \AA . This means that all slits will at minimum cover the common wavelength range 3730 – 5270 \AA , and most will cover from the blue end of the spectrometer sensitivity to the dichroic cutoff. On the red channel, the $\mathcal{R} = 1000$ configuration would cover at least from the dichroic cut on to 7840 \AA . Based on experience, the blue channel wavelength coverage would be more than adequate for redshift identifications for all targeted objects. Information collected on the red side, assuming a dichroic similar to the one assumed, would be very useful for spectral diagnostics but not essential for redshift measurements.

3.4.4 Pre-imaging

It is likely that the proposed survey will be conducted in fields that have been imaged to more than adequate depths using current-generation telescopes (e.g., the CFHT Legacy Survey fields will have very deep images in passbands allowing very clean photometric pre-selection similar to that described above). It should be possible to use astrometry from these external images to design masks to be used for WFOS; in other words, it is

expected that the TMT focal plane (behind the WFOS ADC) will be stable and will be mapped out well enough that no images using WFOS need be taken in order to design slit masks.

3.4.5 Mask design

In this demonstration, we show example mask designs for one arm of one pointing of WFOS centred on the field shown in Figure 15. The mask design software used at this point is a minor variant of software written by K. Adelberger for designing masks for LRIS on the Keck telescope, for objects with similar properties to those proposed here. Briefly, it uses an algorithm based on “simulated annealing” to find a mask of highest total priority (where each object in a catalog has a user-assigned numerical priority) given constraints on the minimum slit length and the maximum fraction of the field in the X (dispersion) direction that may be used (to provide control over the extent of the differences in the wavelengths covered by slits on the same mask). In the test case, slits were allowed to become as short as 4 arcsec (note that this is the \sim the minimum space allocated per object even if nod/shuffle techniques are implemented) and to be placed anywhere within a rectangular field of dimensions $4'.5$ by $6'.4$. The procedure for subsequent masks was to significantly downgrade the priority of objects already assigned to masks before designing the next one, so that an object was repeated only when there was no other object available near the same mask Y position.

The particular pointing shown in Figure 15 has a total of $70\ z = 1.8\text{--}3.5$ candidates to $R(AB) = 24.5$ and 257 candidates with $24.5 < R(AB) \leq 26.5$. (In fact, 38 of the 70 bright candidates in this patch of sky have spectroscopic redshifts already measured to be in the range $1.8 < z < 3.5$.) These numbers correspond to a surface density within the footprint of $\simeq 2.4$ and $\simeq 9.2\ \text{arcmin}^{-2}$ for the “bright” and “faint” subsamples, respectively.

A total of five masks were designed, fixing the location of the footprint and not allowing it to move freely to optimize a given mask. The actual objects assigned to masks are shown in Figure 15. The statistics of these masks are summarized in Table 5. There are several issues to note: first, the number of unique slits assigned is a strongly decreasing function of mask number for a fixed pointing, particularly for the low-surface-density bright sample. Even for objects with a very high surface density such as those targeted in the faint “F” masks, the number of unique objects assigned slits decreases steadily long before the list of potential targets is near exhaustion; after 3 successive mask iterations, one has still covered only about two-thirds of the possible targets within the footprint. Another noteworthy fact: even though slits were allowed to become as short as 4 arcsec, even the first mask targeting faint objects could assign slits to only 70% of the possible number (i.e., the total slit length of 380 arcsec divided by 4 arcsec is 95, not 67). This is in spite of the fact that each $4.5\ \text{arcmin}$ by 4 arcsec swath of the field contains an average of ~ 3 potential faint targets.

The efficiency of assigning unique objects to slits would of course go up if the footprint were dithered in the dispersion direction by some fraction of the $4'.5$ footprint. The dither pattern should be optimized for uniform coverage and a small probability of repeated observations of the same object for the “faint” masks; because of the very limited spectral coverage for the $\mathcal{R} = 5000$ setup, and the lower object density,

Table 6: Mask design statistics, single WFOS barrel with fixed footprint

| Mask name | #Unassigned objects | #Slits assigned | #Repeats | #Unique |
|-----------|---------------------|-----------------|----------|---------|
| B1 | 70 | 40 | 0 | 40 |
| B2 | 30 | 37 | 19 | 18 |
| F1 | 257 | 67 | 0 | 67 |
| F2 | 190 | 62 | 5 | 57 |
| F3 | 133 | 58 | 12 | 46 |

the dither pattern for the bright masks should be forced to re-observe a considerable fraction of the targets with as different “X” positions in spectrometer barrels as can be managed, to provide complementary wavelength coverage. The survey approach would be straightforward for the faint targets (given their nearly complete wavelength coverage in a given observation) but could be complex for the bright ones, depending on the details of the focal plane layout and the precise wavelength coverage in the high resolution mode.

For the present purposes, it is safe to assume that each WFOS pointing will target ~ 270 objects in the “faint” portion of the survey (each requiring 1 hour of integration). The faint survey would thus require ~ 750 pointings in total, or 750 hours (~ 100 nights). Reaching the goal of $\sim 30,000$ high quality sightlines, and assuming that each object must be observed at least twice to obtain good wavelength coverage, the total time required is ~ 6 hours for each set of 160 objects, or a total of 1125 hours (~ 140 nights). *This number could be approximately halved if the observations were made at $\mathcal{R} = 2500$, or if some means of increasing the wavelength coverage at a fixed resolution could be achieved.*

3.4.6 Procedures during the day

The day before the run, the masks for the coming night should be loaded into the cartridge and a through slit image taken with the flat field lamps turned on (no dispersing element). This procedure allows a map to be made of the slit positions so that alignment can be done on each field. This calibration should probably take no more than 5 minutes per mask. We would require that at least 8 masks could be loaded and calibrated in this way in preparation for a given night, but accommodating 10 per barrel is preferable.

3.4.7 Procedures during twilight

No special procedures beyond those given in §4.

3.4.8 Target acquisition

Target acquisition should be done for the four barrels simultaneously in order to minimise overheads. Each mask will have at least 3 alignment apertures (normally boxes, rather than slits) which can be used for fine alignment by being assigned to stars in

the field. Generally stars that are of comparable brightness to the sky background are adequate. It would be ideal if the relative position of the 4 barrels is fixed and a single translation and rotation will align all 4 fields simultaneously. This would require flexure compensation that ties the 4 barrels rigidly together, if such focal plane stability is not achievable mechanically.

Field acquisition could be achieved with the smallest amount of overhead if the on-instrument guider/WFS is tied astrometrically to the science field, so that placing a pre-determined guide star at a pre-determined (x,y) position on the guider field and with the instrument set to the nominal PA will place all reference stars in each barrel within ~ 1 arcsec of the centers of alignment boxes. This would eliminate the need to obtain a short direct image of the field for coarse alignment (a similar scheme is used for field acquisition of the DEIMOS instrument on the Keck II telescope.)

A short direct image ($\sim 10 - 30$ seconds) through the mask would then provide enough information for the instrument software to solve for any small adjustment in PA and in telescope offset. Any rogue reference stars can be rejected interactively by the user through the interface to the alignment software. It should be possible for the entire acquisition to take less than 5 minutes from telescope slew to the start of a science integration.

3.4.9 Target science data acquisition

Our assumptions for the simulated spectra shown in Figures 16 and 17 are that the spectra are taken under dark conditions, with $0''.8$ seeing, $0''.7$ slits and at airmass $\sec z = 1.0$. The resolution is $\mathcal{R} = 5000$ for the primary set-up and $\mathcal{R} = 1000$ for secondary masks.

3.4.10 Calibration data acquisition

No special calibration steps beyond those listed in §4.

3.4.11 Additional requirements

The magazine which houses the masks should be able to store at least 8 pre-cut masks ready for science operation for a given night.

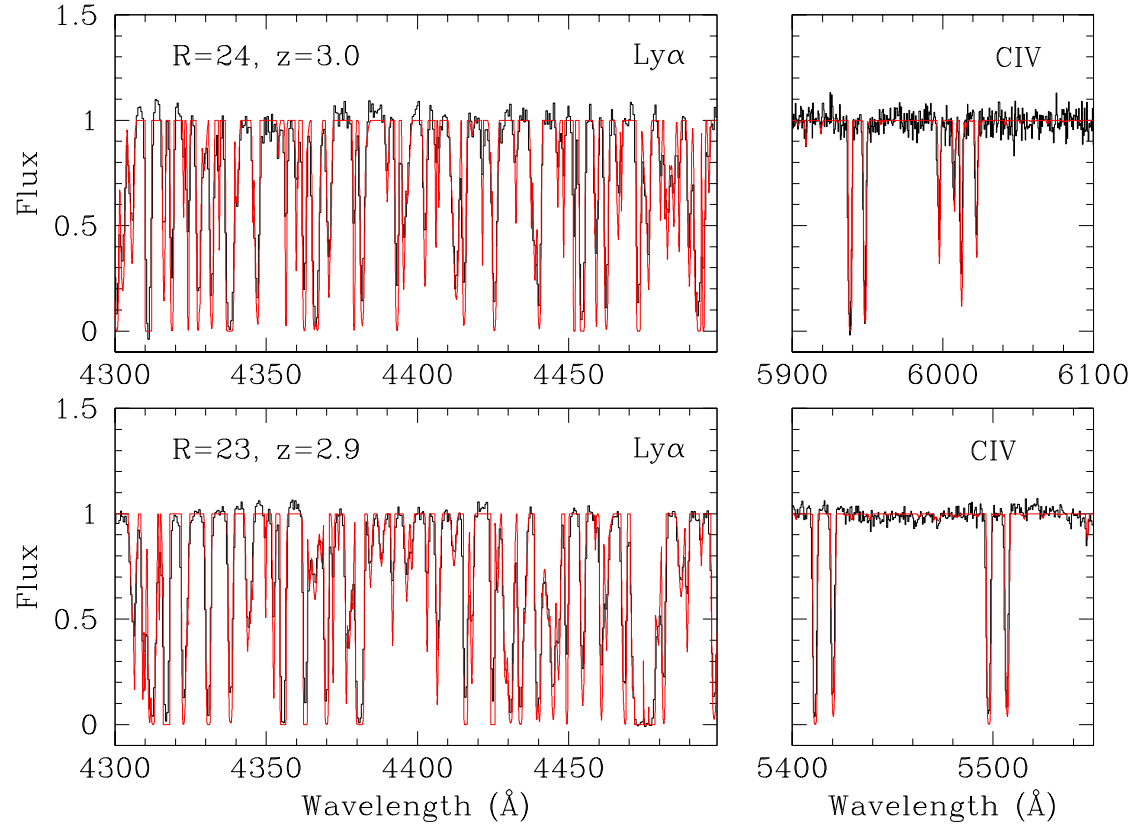


Figure 16: Example sections of simulated spectra for $R(AB) = 23, 24$ $\mathcal{R} = 5000$ configuration. The assumed total integration times were 3 hours. The $\mathcal{R} = 5000$ spectra are black, while the spectra before convolution with the instrumental resolution are shown in red.

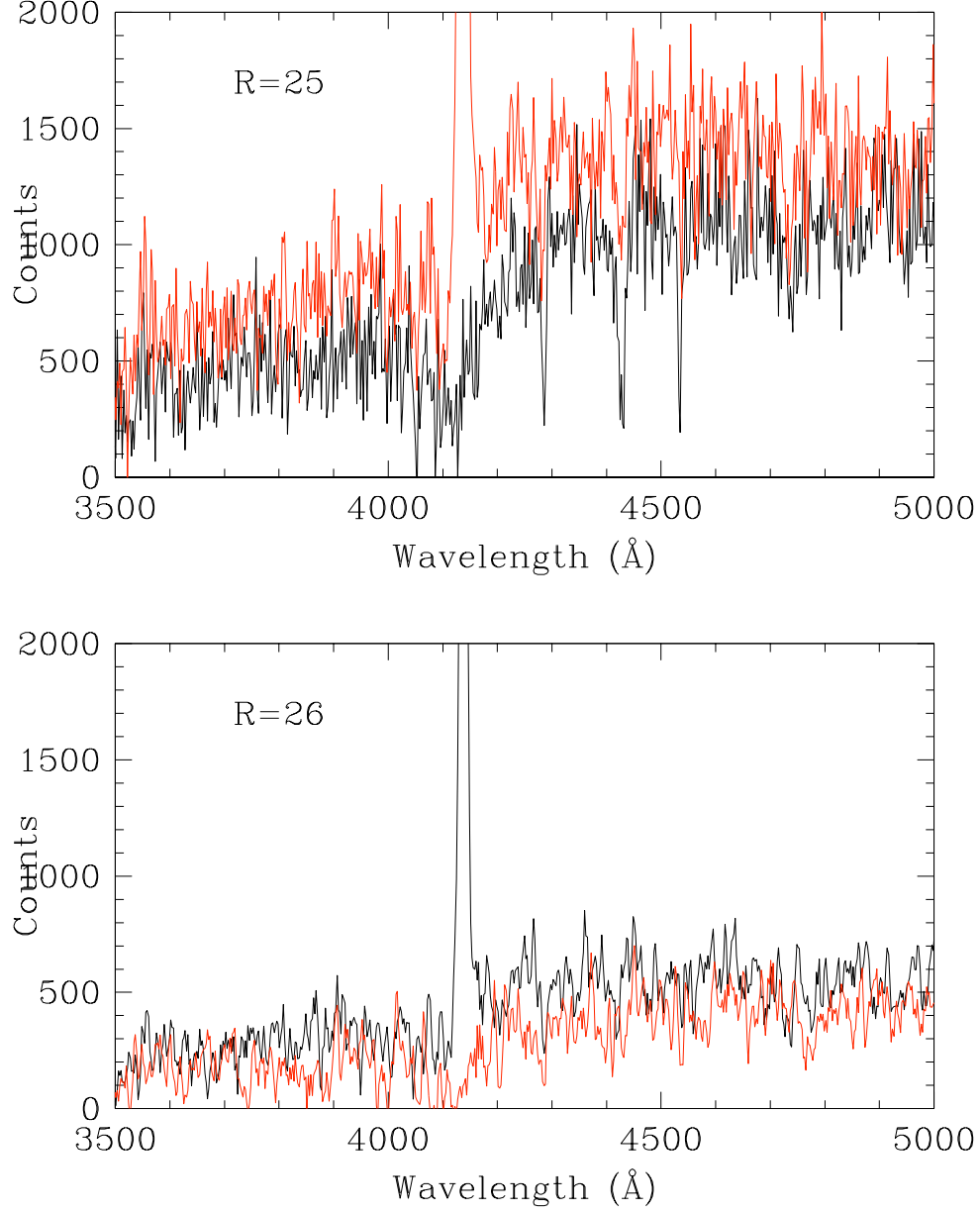


Figure 17: Simulated spectra for $z = 2.4$ galaxies at $R(AB) = 25$ and $R(AB) = 26$, assuming 1 hour total integration time with the blue $\mathcal{R} = 1000$ configuration. The spectra are derived from the composite Lyman break galaxy spectra (Shapley et al. 2003) for the lowest (red) and highest (black) quartiles in Lyman α emission strength. The $R = 26$ spectra will easily yield redshifts even for objects without emission lines. Note that the $R = 26$ spectra have been smoothed with a boxcar filter with a 3 pixel width.

3.5 Astrophysics of primordial galaxies

3.5.1 Science justification and background

A central goal of observational cosmology is to determine how the Cosmic Dark Age was ended by the appearance of First Light: the first luminous self-gravitating objects in the universe. Ultraviolet photons from these objects initiated the epoch of reionization, in which most of the gas in the intergalactic medium left the neutral state, allowing for efficient cooling and the formation of the first galaxies. Despite a wealth of new observational data, we still do not know when reionization occurred, nor do we know what sources are responsible for it. Observations of Gunn-Peterson troughs in quasars show a large neutral HI fraction at $z \sim 6$, leading to early suggestions that reionization occurs (or at least ends) around that redshift. However, the Gunn-Peterson method rapidly saturates when the neutral fraction increases only slightly, and recent WMAP results indicate that reionization may instead have happened somewhere between $z = 10$ and at $z = 20$. A complementary strategy for probing reionization is to focus on the sources of the ionizing radiation, because when reionization occurs we expect a sudden drop by at least a factor of 2 in the number of Ly alpha emitters, accompanied by a sharp reduction in the equivalent widths of detected objects (Rhoads et al 2002). Motivated by this, over the past three years tremendous effort has gone in to determining the abundance of galaxies at $z \sim 6$. At present it seems that the contribution to the cosmic star-formation rate (as measured by UV flux) contributed by galaxies with $L_{UV} > 0.1L^*$ drops a factor of six from $z = 3$ to $z = 6$, falling to $0.005 h_{70} M_{\odot}/\text{yr}/\text{Mpc}^3$ at $z \sim 6$ (Bunker et al. 2004). At this level these objects appear to contribute too few UV photons to reionize the universe. However, the derived ambient flux level of ionizing photons depends on many assumptions, which basically boil down to assuming that star-formation at high redshift occurs in a similar way to how it occurs locally. This is a very unsafe assumption. In fact the following scenarios are all consistent with the data:

1. Reionization occurs (or at least ends) at $z = 6$, and the apparent shortfall in ionizing photons is due to the fact that we are not detecting the sources responsible for the bulk of the ionizing photons (presumably a very abundant population of faint galaxies).
2. Reionization occurs (or at least ends) at $z = 6$, and the apparent shortfall in ionizing photons is because stars at $z = 6$ form with a radically top-heavy stellar initial mass function. This greatly increases the the abundance of ionizing photons produced per unit of star-formation rate.
3. Reionization occurs (or at least ends) at $z = 6$, and the apparent shortfall in ionizing photons is due to a higher-than-expected escape fraction of UV photons from young galaxies. If galaxies at high-redshift are ‘leaky’, the abundance of ionizing photons produced per unit of star-formation rate which escape to the IGM is much higher than predicted on the basis of local observations.
4. Reionization occurs (or at least ends) at $z = 6$, but we are being misled by cosmic variance to underestimate the ambient UV flux.

5. Reionization *is not* occurring at $z = 6$, and is instead occurring at $z \gg 6$, as suggested by the WMAP observations (in fact, the universe may even be multiply re-ionized, c.f. Cen 2003).

All these scenarios are plausible. Progress in testing scenario 4 in the list above (and, to a very limited extent, scenario 5) can be made in the next decade with existing 8–10m telescopes, because they can be tested (to a certain extent) by simply counting galaxies at high redshift. This is effectively the limit of what is possible with present-generation telescopes. But exploring scenarios 1–3 at $z \gtrsim 6$ requires one to measure detailed astrophysical properties (such as the escape fraction and IMF) of galaxies at these redshifts. This is simply beyond the reach of existing telescopes. In this section we will outline a specific set of observations designed to constrain scenario 3 with WFOS.

3.5.2 Key observable: the escape fraction of UV photons at $z \sim 6$

A central measurement linking galaxies to the intergalactic medium at the epoch of reionization is the efficiency with which an ultraviolet photon produced by a young star can escape the galaxy in order to photoionize an atom of neutral hydrogen in the intergalactic medium. For concreteness, we will adopt a slightly modified⁵ version of the definition of the escape fraction, f_{esc} , given in Steidel, Pettini & Adelberger (2001), and parameterize the escape fraction using as the fraction of photons at 900 Å which escape the galaxy without being absorbed, f_{900} , relative to the fraction of photons at 1100 Å which escape the galaxy without being absorbed, f_{1100} :

$$f_{esc} = \frac{f_{900}^{observed} / f_{900}^{emitted}}{f_{1100}^{observed} / f_{1100}^{emitted}} \quad (1)$$

Both $f_{900}^{observed}$ and $f_{1100}^{observed}$ are measured directly from a rest-frame ultraviolet spectrum, but before being used in Equation 1 these raw measurements must be corrected for the intergalactic absorption along the line of sight to the galaxy. Determining this correction can be quite involved⁶, but for present purposes our goal is simply to ensure that we obtain WFOS spectra with reasonable signal-to-noise at rest wavelengths 900 Å and 1100 Å, so that we have something worth correcting. Operationally, f_{900} will be measured by computing the mean flux over the wavelength range 880 Å — 910 Å and f_{1100} will be measured by computing the mean flux over 1120 Å — 1170 Å.

3.5.3 Sample definition

The observations undertaken for this science program will require extensive very deep imaging in order to define a target sample of $z \sim 6$ galaxies using continuum breaks.

⁵Steidel, Pettini & Adelberger (2001) define f_{esc} using flux ratios at rest wavelengths 900 Å and 1500 Å, instead of our chosen channels at rest 900 Å and 1100 Å. Although the spectrum at 1500 Å is somewhat cleaner than that at 1100 Å, 1500 Å at $z = 7$ corresponds to 1.2 μm, which is inaccessible to the red arm of the visible-wavelength channel of WFOS.

⁶See Steidel, Pettini & Adelberger (2001) for one approach to making the correction, based on using a template quasar spectrum as a reference. It is also worth noting that both $f_{900}^{emitted}$ and $f_{1100}^{emitted}$, which also appear in Equation 1, must come from a model.

Images to the required depth can already be obtained using the Hubble Space Telescope, although the field of view of ACS is only $\sim 11 \text{ arcmin}^2$, so it may be that JWST will be needed in order to obtain imaging over the full field of view of WFOS. In any case, existing data obtained from the Hubble Ultra-Deep Field campaign suggests that the surface density of sources at $z \sim 6$ will be $\sim 1 \text{ arcmin}^{-2}$ to 27 mag (AB) at around $1 \mu\text{m}$ (Yan & Windhorst 2004; Bunker et al 2004). Assuming a total WFOS field-of-view 100 arcmin^2 , and assuming that about 2/3 of the sample will be observable after allowing for spectrum overlaps, about 70 objects will be observed simultaneously. Assuming 0.5 arcsec slits (see below), the positions of these candidates will need to be known to an astrometric precision of $\lesssim 0''.05$.

3.5.4 Pre-imaging

Pre-imaging is *not* required for this program. The candidate galaxies are unlikely to be visible in pre-imaging observations, and the positions of the targets will need to be established on the basis of the images obtained at other facilities that will be used in order to define the sample. Pre-imaging observations will only be absolutely essential if the geometrical distortions of the spectrograph are not well characterized prior to mask design. A short (5 minute) pre-imaging observation might be somewhat useful to discard mask alignment stars with large proper motions. However, as will be described below, enough alignment stars will be available on the masks to allow high proper motion stars to be discarded anyway, simply by inspection during the mask alignment phase of target acquisition.

3.5.5 Mask design

Because of the limited precision of photometric redshifts, we will construct our masks to probe targets spanning the redshift range $5.5 < z < 6.5$. The required wavelength coverage is bounded on the blue side by $\lambda_{rest} = 880 \text{ \AA}$ at $z = 5.5$, and on the red side by $\lambda_{rest} = 1170 \text{ \AA}$ at $z = 6.5$. This corresponds to a $\sim 3100 \text{ \AA}$ -wide observed wavelength range spanning $5700 - 8775 \text{ \AA}$. We will use a broad-band filter to limit transmission within this range. The best choice for spectral resolution is $\mathcal{R} = 1000$ (with a $0''.75$ slit). The instrumental configuration will have a central wavelength of 7000 \AA , and a dispersion of $\sim 0.66 \text{ \AA/pixel}$ with the nominal detector. The wavelength range of interest spans about 4700 pixels on the detector (unbinned), which is about half the physical size of the mosaiced array in the dispersion direction. In principle two tiers of targets will be possible, though in practice our source density will be low enough that two tiers will not be necessary. The targets are small with full-widths of around $0''.5$, so two masks will be cut with slit widths of $0''.5$ and $0''.75$. The specific mask used will depend on seeing conditions. Because the density of targets is relatively low, a ‘Case 1’ nod & shuffle strategy (see Abraham et al. 2004) will be assumed when distributing the slits across the targets. In other words, the slit length will be twice the slit width, allowing room for the targets to be located in two positions on the slit as part of the nod & shuffle sky subtraction. However, when designing the mask a virtual slit length of four times the slit width will be assumed so that sufficient detector area is available to store charge from two object positions and two sky positions. Each mask

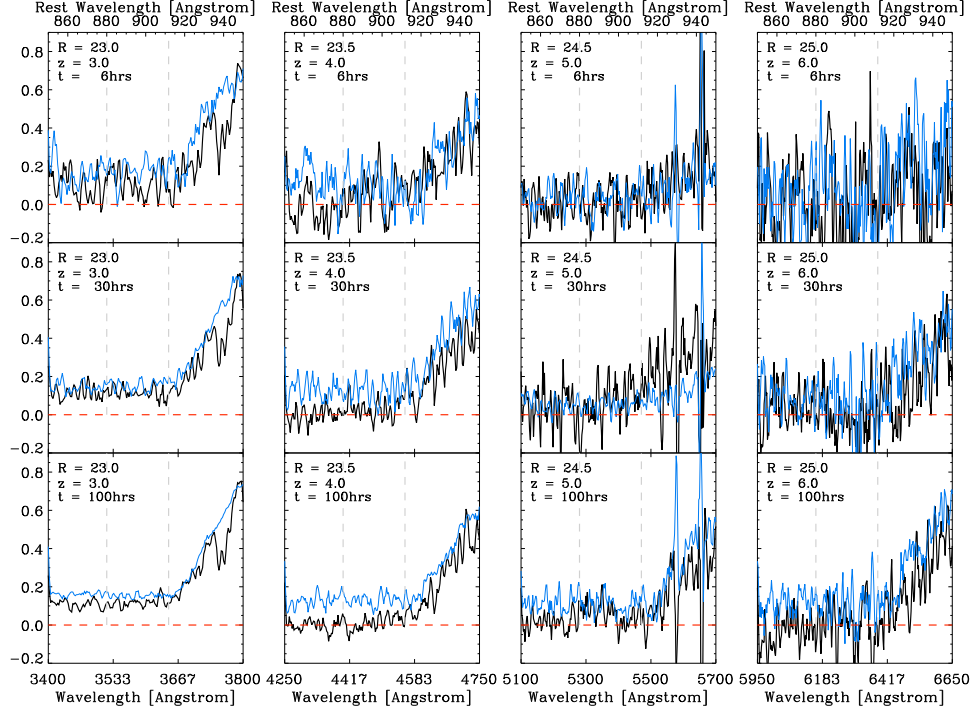


Figure 18: Simulation showing a synthetic WFOS observation of the rest UV spectrum of a young galaxy at $z = 3, 4, 5$, and 6 (left to right). The apparent magnitude of the galaxy at these redshifts is $R = 23.0, 23.5, 24.5$, and 25.0 , respectively, and a constant star-formation rate is assumed. Exposure times of $6h, 30h$, and $100h$ are shown (top to bottom). The black curve shows the synthetic measured spectrum, while the blue spectrum shows what the measured spectrum would have been in the absence of foreground absorption systems. Dashed lines mark the region contained within the 880\AA to 910\AA window used to measure continuum leakage.

should contain holes for a minimum of seven mask alignment stars.

3.5.6 Required integration time

In order to determine the required integration time we simulated spectra of young galaxies seen at high redshift with flux attenuated by foreground absorption systems. Absorption was modeled using the Lyman α forest parameters derived by Ellison et al (1999) for a $z = 3.7$ APM quasar (which had 380 absorption systems over a redshift width $\Delta z = 0.7$). The number of absorbers was scaled to increase with redshift according to $(1+z)^{1.5}$. We drew random redshifts, and also randomly drew the properties of individual absorbers from the list in Ellison et al. (1999).

The apparent magnitude of the primordial galaxy being modeled was assumed to be $R = 23.0, 23.5, 24.5$, and 25.0 , at $z = 3, 4, 5$, and 6 , respectively. A constant star-formation rate was assumed, although the results were not sensitive to the model

prescription, so long as the galaxy was actively star forming. In fact it was found that the distribution of Lyman alpha forest clouds played a far more dominant role in conditioning the observability of continuum in the 880\AA to 910\AA window, so that continuum visibility varied strongly from realization to realization for galaxies at the same redshift and magnitude. We included no intrinsic absorption in the galaxy since our goal was to model a leaky system. Figure 18 shows a set of realizations corresponding to exposure times of 6h, 30h, and 100h with WFOS. For the specific realizations shown (drawn entirely at random), continuum in this individual object is obvious in the 6h integration at $z = 3$ and in the 30h integration at $z = 5$, but nearly invisible even in 100h at $z = 4$ and $z = 6$ (in the former case simply because of an unfortunate distribution of foreground absorbers, and in the latter case because of both the distribution of absorbers and the faintness of the underlying continuum).

On the basis of these simulations, we conclude that exposure times of 50–100 hours will be needed to obtain measurements for individual objects in the range $5 < z < 6$, and that if galaxies are leaky then continuum detections will be made for individual bright galaxies with ‘lucky’ sight-lines with few nearby foreground absorbers, or where a strong proximity effect is in place. Detections based on composite co-additions of all spectra will yield interesting constraints for the sample as a whole. Since a single observation of the 100 arcmin^2 WFOS field-of-view will yield about 50 targets, a single pointing will contain enough objects to allow us to construct a high signal-to-noise composite spectrum.

3.5.7 Procedures during the day

No special requirements beyond those given in Section 4.

3.5.8 Procedures during twilight

None required.

3.5.9 Target acquisition

Identical to the procedure given in §3.4.8.

3.5.10 Sky subtraction, CCD device characteristics, and shutter operation

Over the course of the 20 nights needed to complete this program each camera shutter will operate ~ 15000 times. An additional requirement placed on WFOS by these observations is that the lifetime of the camera shutters remain long even in the face of this kind of usage. Because the charge will also be shuffled on the detector ~ 15000 times, it is essential that the detectors have both very good charge transfer efficiency and minimal lattice defects.

These defects manifest themselves as ‘charge traps’ in the shuffled images (short pairs of streaks perpendicular to the shuffle direction, separated by the shuffle distance). We believe these charge traps occur because detector defects are pumped by the shuffle-and-pause action. If the acquisition of detectors free of such defects cannot be assured,

then an additional requirement on WFOS should be that a detector translation assembly be built into the spectrograph. Charge traps always appear at the same place on the CCD, so their undesired effect can be greatly reduced by dithering the image along the spatial axis and rejecting outliers during stacking. Additional offsets can be applied between exposures in order to position the image on different pixels on the array.

The detector should also be chosen to have minimal charge diffusion. Charge diffusion increases exponentially with wavelength and is important to eliminate because extremely faint target spectra will be stored immediately adjacent to extremely strong sky spectra on the CCD. While the effect can be reduced or avoided by increasing the distance between the object and sky in the shuffle, this would be done at the cost of less efficient use of the detector area, and it would be better to minimize the problem by ensuring the architecture of the detectors has minimal charge diffusion to begin with.

3.5.11 Calibration data acquisition

No special requirements beyond those given in Section 4.

3.5.12 Facility requirements

The nod time of the Nod & Shuffle sky subtraction process will have to be short ($\sim 20 - 30$ s) to allow sky removal to be undertaken at the level of precision required. The OIWFS on WFOS and the telescope control system must be designed so that handshaking between the telescope and spectrograph is very efficient and introduces minimal overheads. A two-second overhead should be the maximum allowed, in order to ensure a $< 10\%$ penalty when using Nod & Shuffle.

This project would benefit from being undertaken in a queue. Since the appropriate dichroic may not be in place for this program, capability to rapidly change dichroics is a requirement. The magazine which houses the masks should be able to store at least enough pre-cut masks (at least 10) that the masks for this project can be stored along with the masks for other programs in the queue.

4 Calibration Procedures

4.1 Geometric distortion

For multi-aperture spectroscopy with WFOS it is important to determine the transformations needed to map sky coordinates to the wavefront sensor position, mask location, and the detector plane. These transformations are required for a number of reasons including: (a) the determination of slit positions from image data to facilitate mask design; (b) the correct calculation of telescope offsets from displacements measured at the detector to facilitate acquisition and (c) to ensure that the acquisition stars appear within the holes in the mask during the initial telescope pointing. In general, these transformations will have a chromatic component. The mask-detector transformation can be deduced by taking images through each mask loaded in the mask changer and comparing the expected positions of the apertures with those predicted if the mask and its mounting were perfect. For example, this may account for shifts in the way that the mask is mounted in its holder. This may need to be re-determined every time a new mask is introduced into the instrument and would normally be a daytime operation. The wavefront sensor-to-detector transformation is determined by taking images through a matrix mask in different passbands. The sky-detector transformation is determined by taking images of fields with very accurate pre-existing astrometry. Both the wavefront sensor-to-detector and sky-to-detector transformations will be determined during commissioning and periodically re-checked. A requirement is that these transformations remain stable on a time scale of months-to-years.

4.2 Flat-field and bias

Flat-field observations calibrate the relative (pixel-to-pixel) response of the each pixel of the detector. The bias is taken with no light incident on the detector to determine the electronic bias level. This might also provide some check on the CCD gain. For spectroscopy, it will be necessary to determine the flat-field correction with dispersed white light for each combination of mask, dichroic and disperser. This is so that each pixel receives light of the correct wavelength as it experiences in the on-target exposures. In this way, fringing effects can be removed (in the absence of instrument flexure). It also provides a more accurate calibration of the vignetting function since this depends on the dispersion configuration. In most cases, the flat-field exposures will be done during the daytime setup using a script to automate the process for each spectrograph. A facility requirement imposed by the need for this calibration procedure is that the interior of the dome must contain a large screen (or at least an area with flat matte white paint-work) and an illumination lamp.

In exceptional cases, where fringing is a problem but Nod & Shuffle mode will not be used to eliminate fringes, it might be necessary to obtain flat-field calibrations on-sky while tracking the target field to eliminate flexure problems. If the spatial uniformity of the calibration light is not sufficient to measure large-scale non-uniformity (due to e.g. vignetting) this information will be obtained from observations of blank regions of sky.

Bias frames needed to remove reset pedestal in the visible-wavelength detectors

will be constructed by median combining 20-30 zero-second bias frames. These will be obtained regularly during the afternoon using simple scripts. Dark current removal will be described below.

4.3 Wavelength calibration

For observations requiring accurate wavelength determination, it may be necessary to take calibration exposures while tracking the target field so as to eliminate the effect of instrument flexure. In the most demanding cases, it will be necessary to interleave these exposures with exposures of the target field so that effect of the flexure can be measured and accounted for in the data reduction. A requirement imposed by this is that the calibration lamp pick-off mirrors can be inserted and removed from the optical path quickly (at most a few tens of seconds) so as to avoid adding significant overheads.

In cases where very accurate wavelength calibration is not required, it may be sufficient to carry out the wavelength calibration observations at the start of the night (perhaps during the day) or at intervals while the telescope is parked. The best strategy for a given observation depends critically on the amount of instrument flexure. Note that this calibration will not remove wavelength errors caused by tracking (which causes the target to move with respect to the slit) since the calibration system will not be able to reproduce this effect. In all cases, the calibration observation would be done with the same mask and dispersion configuration used for the observations of the target field. Supplemental wavelength calibration may also be available using sky lines. For example, at wavelengths longwards of $0.7\mu\text{m}$ there are a large number of telluric emission lines which can be used for wavelength calibration.

4.4 Flux calibration

Flux calibration is needed to reduce spectra to a relative or absolute scale of flux density. For relative flux calibration, it is necessary to observe a spectrophotometric standard star. This should be observed at the same airmass to avoid errors due to differential extinction. (If for some reason the WFOS ADCs were not used, this would also be important to ensure that wavelength-dependent slit losses were the same for the standard and target observations.) Certain programs will require absolute flux calibration, in which case it will be necessary to observe both the target and standard with a very wide slit so as to admit all the light. Again, it will be necessary to observe both at the same airmass so that the atmospheric extinction is the same.

In general, flux calibration standards will be observed after a complete sequence of observations of the same field, perhaps just once or twice per night. Usually, it will be sufficient to observe the standard star with a generic single-aperture mask. Any systematic difference in flux calibration over the field, because of vignetting, for example, would be accounted for in the flat-field calibration. A requirement imposed by the need for flux calibration is that the mask holder have enough positions that a long-slit mask (containing parallel long-slits at a range of slit widths from $0''.2$ to $2''.0$) can be permanently included in the suite of masks available throughout the night.

4.5 Linearity

The linearity of the both visible-light and infrared detectors should be verified by taking a series of exposures of a constant flux source at varying exposure times. A requirement on the WFOS detectors and electronics is that linearity test exposures should not be required to be undertaken more often than a few times per year.

Because IR detectors are sensitive to variations in capacitance at detector nodes as charge collects on these nodes, additional steps will be needed to calibrate the detectors in the IR arm of WFOS. In general, these detectors should be operated so that science data is taken at no more than half of the full-well capacity of the array. A requirement on the detectors is that when they are operated at less than half full-well, deviations from linearity will be less than 10%. Because calibration at the 10% level will usually be inadequate, linearity corrections will still be needed. A requirement on the operation of WFOS is that linearity corrections accurate to within 10% are always available, so that these can be applied to the data frames to calibrate the linearity of the data to a final precision of 1%. A requirement on the WFOS software is that (as a transparent first step in data reduction) all images from the IR detectors are automatically linearized using a master linearity correction frame, and that details of this procedure are noted in the frame header so that the procedure can be easily reversed. A requirement on the facility is that the master linearity correction frame applied to the data in the background is both supplied with the final data product and permanently archived at a central location. Because linearity of IR arrays can be a function of ambient temperature, a requirement imposed on WFOS by the need for this calibration is that the ambient temperature of the detector at the time of observation is recorded in each frame header.

4.6 Dark current

Bias frames and the overscan regions of the CCD detectors in the red and blue arms can be used to remove reset pedestals from the data, but in general the calibration frames needed to remove a combination of dark current and pedestal can not simply be simply constructed from a short bias image plus a long dark exposure scaled to the appropriate exposure time. Because dark current can be significant for the IR arrays, dark images should be obtained with identical array operating conditions (exposure time, number of readouts, etc.) as the science exposures they will be used for. Subtraction of a dark image will remove any reset pedestal and dark current. A requirement imposed on the instrument by the need for obtaining dark images is that a very light-tight environment exists internally within WFOS so that dark images can be obtained in the afternoon even when the dome is fully illuminated.

4.7 Telluric absorption

Many spectroscopic observations require correction for telluric absorption. Such absorption corrections can be obtained from spectra of stars with known spectral type. For programs in which the telluric correction is critically important, observations of calibration stars at the same airmass as the object should bracket the observation of the object. To remove intrinsic stellar features the calibration star spectra should be

divided by model atmospheres or observed spectra which have been convolved to the same resolution as the WFOS data. These stellar feature corrected spectra can then be used to correct the object spectra for telluric absorption.

5 Summary: Building the Spectrograph We Want

Table 6 presents a flow-down summary of the science requirements contained within this document. In this section the Science Team will offer some suggestions for improvements to the design and some final thoughts on the optional components of the spectrograph,

5.1 Desired improvements

A number of general improvements to the spectrograph design should be considered:

- *Increase maximum spectral resolution to $R = 7500$.* While a hard limit on spectral resolution is imposed by polarization effects in the VPH gratings (which rule out $R \sim 10000$), at slightly lower resolutions ($R = 7500$) the limits seems to be imposed by mechanical issues (with regard to larger camera swing arcs) and manufacturing issues (with regard to larger gratings). Dealing with these seems hard but we *really* want higher resolution, so we suggest that the engineering team examine more closely various possibilities for improving the mechanics of the spectrograph to allow higher resolution.
- *Look into improving the wavelength stability specification.* We think we (the Science Team) need to think a little harder about the wavelength stability specification to make sure that the current design delivers enough stability. If not, we might recommend the engineering team look into some more sophisticated flexure modeling/correction. For example, IMACS on Magellan has a nice system in which small apertures on one or both sides of the masks monitor the position a single strong sky line on an independently read-out auxiliary chip flanking the science detectors. Centroiding the line at a given position on these chips allows flexure to be monitored to sub-pixel accuracy, and a closed-loop flexure correction can be implemented by moving the piezo-electric stage that holds the CCDs.
- *Add a CCD translation stage to each of the barrels.* Movable CCD stages are essential because dithering between exposures provides a backstop correction for Nod & Shuffle artifacts introduced by chip defects (see §3.5.10).
- *We need to think more about how we are going to undertake calibrations.* Since TMT will not have a facility calibration system, more thought needs to be put into how we will undertake some aspects of calibration. For example, will a giant screen on the dome really be needed for dome flats, or can some diffuse illumination be fed into the spectrograph in some other way?

5.2 Science value of GLAO to WFOS

To demonstrate the benefits of GLAO, we briefly consider the impact of its implementation on a single science program from §3 — the measurement of the dark matter

distribution in the elliptical galaxy M49 using WFOS velocities for its globular clusters (GCs) and planetary nebulae (PNe).

Since GCs and PNe at the distance of M49 are unresolved — and almost always much fainter than the combined sky+galaxy background — GLAO would prove advantageous for this program. The exposure time calculations in §3.3 are based on an assumed FWHM of $0''.8$ at a wavelength of $0.5\mu\text{m}$, which is intermediate to the “typical” and “bad” ground-layer profiles. GLAO is expected to deliver a 15–20% improvement in FWHM at this wavelength, and a commensurate reduction in the integration time needed to achieve the target signal-to-noise ratio of $S/N \approx 1$ per \AA . Thus, the total open-shutter time needed to measure radial velocities for 4000 GCs and 1000 PNe in M49 would be reduced from 19 to 16 hours. If one aims to accumulate radial velocity samples of 1000 or more GCs in ~ 50 galaxies, the savings amount to ~ 2.5 nights over the course of the original 15-night program.

5.3 Science value of IR arm to WFOS

TBA

5.4 GLAO vs. SLGLAO

TBA

5.5 Future changes in this document

This document will evolve as the WFOS design evolves, until completion of the design study. The next version of this document will incorporate a case for the the proposed infrared arm, and possibly a pure imaging case.

Table 7: Flow-down of Science Case Requirements

| | White dwarfs | Resolved populations | Dark matter mapping | IGM Tomography I | IGM Tomography II | High-z escape fraction |
|---|--------------|----------------------|---------------------|------------------|-------------------|------------------------|
| Slits/mask | 200 | 380 | 100–750 | 40 | 70 | 50 |
| Masks/barrel/night | 2 | 2,5,7 | 6 | 2 | 10 | 2 |
| Slit width [arcsec] | 0.6 | 0.8 | 0.6 | 0.75 | 0.75 | 0.75 |
| Number of nights required | 3 | 28 | 15 | 40 | 100 | 20 |
| Typical integration time/exposure [s] | 1800 | 1200 | 1200 | 1800 | 1800 | 1800 |
| Typical integration time/mask [ks] | 15 | 9,3 | 3.6 | 22 | 3.6 | 200 |
| Resolution (blue arm/red arm) | 2000 | 5000 | 2000/5000 | 5000 | 1000 | 1000 |
| Number of dichroics needed | 1 | 1 | 1 | 2 | 1 | 1 |
| Good wavelength for dichroic split [Å] | 5800 | 6000 | 6000 | 4300/5000 | 5600 | 5500 |
| Minimum wavelength (blue arm/red arm) [Å] | 3400 | 4600/7900 | 3700/8300 | 3400/4300 | 3200/5600 | 5700 |
| ... when second dichroic is used: | – | – | – | 4400/5000 | – | 5700 |
| Maximum wavelength (blue arm/red arm) [Å] | 5800 | 5200/9000 | 5400/8800 | 4300/5400 | 5600/10300 | 8775 |
| ... when second dichroic is used: | – | – | – | 5000/6400 | – | 5700 |
| Seeing FWHM required [arcsec] | 0.7 | 0.8 | 0.8 | 0.8 | 0.8 | 0.75 |
| Needs pre-imaging? | ✓ | ✓ | ✓ | | | |
| Calibrate with sky lines? | | | | | ✓ | ✓ |
| Need very precise flux calibration? | | ✓ | ✓ | | | |
| Needs very precise sky subtraction? | | ✓ | ✓ | ✓ | ✓ | ✓ |
| Benefits from Nod & Shuffle? | | ✓ | ✓ | ✓ | ✓ | ✓ |
| Best done in a queue? | ✓ | | ✓ | ✓ | ✓ | ✓ |
| Uses blue and red arms at same time? | ✓ | ✓ | ✓ | ✓ | ✓ | |
| Big benefits from GLAO? | ✓ | ✓ | ✓ | ✓ | ✓ | ✓ |
| Big benefits from SLGLAO? | ✓ | ✓ | ✓ | | | |
| Care about LGS beacon positions? | ✓ | | ✓ | | | |
| Benefits from quick switch of dichroics? | | | | ✓ | ✓ | ✓ |
| Efficiency a strong function of dichroic split? | | | | ✓ | ✓ | ✓ |
| Hurt by non-contiguous coverage? | ✓ | ✓ | ✓ | | | |
| Synergistic with JWST? | | ✓ | | ✓ | ✓ | ✓ |
| Synergistic with ALMA? | | | | ✓ | ✓ | |

6 References

- Abraham, R.G., et al. 2004, *Aj*, 127, 2455
Adelberger, K.L. 2004, *ApJ*, 612, 706
Bedin, L. et al. 2005, *ApJL*, 624, 45
Bergeron, P., Ruiz, M., & Leggett, S. 1997, *ApJS*, 108, 339
Bergeron, P., Wesemael, F., & Beauchamp, A. 1995, *PASP*, 107, 1047
Bergeron, P., Saffer, R., & Liebert, J. 1992, *ApJ*, 394, 228
Bunker, A.J., Stanway, E.R., Ellis, R.S., & McMahon, R.G. 2004, *MNRAS*, 355, 374
Bullock, J.S., Kravtsov, A.V., & Weinberg, D.H. 2001, *ApJ*, 548, 33
Bullock, J.S., & Johnston, K.V. 2005, *ApJ*, submitted. (astro-ph/0506467)
Cen, R. 2003, *ApJ*, 591, 12
Choi, P.I., Guhathakurta, P., & Johnston, K.V. 2002, *AJ*, 124, 310
Côté, P., Oke, J.B., & Cohen, J.G. 1999, *AJ*, 118, 1645
Côté, P., et al. 2001, *ApJ*, 559, 828
Côté, P., McLaughlin, D.E., Cohen, J.G., & Blakeslee, J.P. 2003, *ApJ*, 591, 850
D'Antona, F. 2001, *IAU Symposium Series*, Extragalactic Star Clusters, 207
Ellison, S.L., et al. 1999, *PASP*, 111, 946
Ferguson, A.M.N., Irwin, M.J., Ibata, R.A., Lewis, G.F., & Tanvir, N.R. 2002, *AJ*, 124, 1452
Font, A.S., Johnston, K.V., Bullock, J.S., & Robertson, B. 2005, *ApJ*, submitted. (astro-ph/0507114)
Geha, M.C., Guhathakurta, P., Rich, R.M., & Cooper, M.C. 2005, *AJ*, in preparation
Guhathakurta, P., et al. 2005, *Nature*, submitted. (astro-ph/0502366)
Guhathakurta, P., et al. 2005, *AJ*, submitted. (astro-ph/0406145)
Hansen, B. et al. 2004, *ApJS*, 155, 551
Hansen, B. et al. 2002, *ApJL*, 574, 155
Ibata, R., et al. 2004, *MNRAS*, 351, 117
Kalirai, J. et al. 2005a, *ApJL*, 618, 123
Kalirai, J. et al. 2005b, *ApJL*, 618, 129
Kalirai, J. et al. 2001b, *AJ*, 122, 3239
Kalirai, J. et al. 2001a, *AJ*, 122, 257
Kleinman, S. et al. 2004, *ApJ*, 607, 426
Krauss, L. & Chaboyer, B. 2003, *Science*, 299, 5603, 65
Merritt, D., & Tremblay, B. 1993, *AJ*, 106, 2229
Monelli, M. et al. 2005, *ApJL*, 621, 117
Napolitano, N.R., et al. 2005, *MNRAS*, 357, 691
Peng, E.W., Ford, H.C., & Freeman, K.C. 2004, *ApJ*, 602, 705
Pettini, M., et al. 2002, *ApJ*, 569, 742
Reitzel, D.B., & Guhathakurta, P. 2002, *AJ*, 124, 234
Reitzel, D.B., Guhathakurta, P., & Rich, R.M. 2004, *AJ*, 127, 2133
Richer, H. et al. 2005, in preparation
Richer, H. et al. 2004, *AJ*, 127, 2771
Richtler, T., et al. 2003a, *AJ*, 127, 2094
Rhoads, J.E., et al. 2003, *AJ*, 125, 1006
Schiavon, R.P., & Barbuy, B. 1999, *ApJ*, 510, 934

Somerville, R. & Primack, J. 1999, MNRAS, 310, 1087
Steidel, C.C., et al. 2004, ApJ, 604, 534
Steidel, C.C., Pettini, M., & Adelberger, K.L. 2001, ApJ, 546, 665
van den Bergh, S. & Tammann, G. 1991, ARA&A, 29, 363
Weidemann, V. 2000, A&A, 363, 647
Yan, H., & Windhorst, R.A. 2004, ApJ, 600, L1